REPORT DOCUMENTATION PAGE

Form Approved OMB NO. 0704-0188

1. REPORT DATE (DD-MM-YYYY)	2. REPORT TYPE	3. DATES COVERED (From - To)
23-08-2021	Book Chapter	-

4. TITLE AND SUBTITLE
Distortional hardening cyclic plasticity: Experiments and modeling

5a. CONTRACT NUMBER
W911NF-19-1-0040

5b. GRANT NUMBER

5c. PROGRAM ELEMENT NUMBER
611102

6. AUTHORS
René Marek, Slavomír Parma, and Heidi P. Feigenbaum

5d. PROJECT NUMBER

5e. TASK NUMBER

5f. WORK UNIT NUMBER

7. PERFORMING ORGANIZATION NAMES AND ADDRESSES
Northern Arizona University
PO Box 4130
1298 S. Knoles Drive, Bldg 56, Ste. 240
Flagstaff, AZ 86011 -4130

8. PERFORMING ORGANIZATION REPORT NUMBER

9. SPONSORING/MONITORING AGENCY NAME(S) AND ADDRESS (ES)
U.S. Army Research Office
P.O. Box 12211
Research Triangle Park, NC 27709-2211

10. SPONSOR/MONITOR'S ACRONYM(S)
ARO

11. SPONSOR/MONITOR'S REPORT NUMBER(S)
73337-EG-H.5

12. DISTRIBUTION AVAILIBILITY STATEMENT

13. SUPPLEMENTARY NOTES
The views, opinions and/or findings contained in this report are those of the author(s) and should not contrued as an official Department of the Army position, policy or decision, unless so designated by other documentation.

14. ABSTRACT

15. SUBJECT TERMS

16. SECURITY CLASSIFICATION OF:			17. LIMITATION OF ABSTRACT	15. NUMBER OF PAGES	19a. NAME OF RESPONSIBLE PERSON
a. REPORT	b. ABSTRACT	c. THIS PAGE			Heidi Feigenbaum
					19b. TELEPHONE NUMBER: 928-523-5326

REPORT DOCUMENTATION PAGE (SF298)
(Continuation Sheet)

Continuation for Block 13

Proposal/Report Number: 73337.5-EG-H

Report Title: Distortional hardening cyclic plasticity: Experiments and modeling
Report Type: Book Chapter

Publication Type: Book Chapter Peer Reviewed: Y **Publication Status:** 2-Awaiting Publicat
Chapter Title: Distortional hardening cyclic plasticity: Experiments and modeling
Publication Identifier Type: Publication Identifier: https://doi.org/10.1016/B978-0-12-819293-1.
Volume: Edition: 1st Page#:
Date Received: 23-Aug-2021 Publication Year: 2021
Publisher: Elsevier
Publication Location:
Book Title: Cyclic Plasticity of Metals
Authors: René Marek, Slavomír Parma, and Heidi P. Feigenbaum
Editor: Hamid Jahed and Ali Roostaei
Acknowledged Federal Support: **Y**

AUTHOR QUERY FORM

ELSEVIER	**Book:** Elsevier Series on Plasticity of Materials **Chapter:** 06	**Please e-mail your responses and any corrections to:** **E-mail:** s.jayachandran@elsevier.com

Dear Author,

Please check your proof carefully and mark all corrections at the appropriate place in the proof. **It is crucial that you NOT make direct edits to the PDF using the editing tools as doing so could lead us to overlook your desired changes.** Rather, please request corrections by using the tools in the Comment pane to annotate the PDF and call out the changes you would like to see. To ensure fast publication of your paper please return your corrections within 48 hours.

For correction or revision of any artwork, please consult http://www.elsevier.com/artworkinstructions

Any queries or remarks that have arisen during the processing of your manuscript are listed below and highlighted by flags in the proof.

Location in chapter	Query / Remark: Click on the Q link to find the query's location in text Please insert your reply or correction at the corresponding line in the proof
Q1	There was a remark "Search "XX" for inline comments requiring attention" for the file 2018_Lester_Scherzinger.bib. It is not clear what inline comments the author is indicating, please clarify. (p. 224/ line 19)

Please check this box or indicate your approval if you have no corrections to make to the PDF file ☐

Thank you for your assistance.

B978-0-12-819293-1.00016-4, 00006

Distortional hardening cyclic plasticity

Experiments and modeling

6

René Marek[a], *Slavomír Parma*[a], *and Heidi P. Feigenbaum*[b]
[a]Institute of Thermomechanics, Czech Academy of Sciences, Prague, Czech Republic,
[b]Department of Mechanical Engineering, Northern Arizona University, Flagstaff, AZ, United States

6.1 Introduction

As the yield surface (YS) can be employed to stipulate operating states and conditions of machine components and structures, as well as to predict the elasto-plastic flow of material, it is crucial that it is accurately captured experimentally and mathematically. While it has been well established that YS can change size and translate due to plastic straining, it is less known that YS often also distorts due to strain hardening. The distortion of the YS has been observed in numerous experiments on various types of metals dating back over 60 years.

The distortion of the YS in stress space can change the von Mises circle into either an ellipse or into a more complex shape featuring high curvature in the direction of loading—often with a sharp apex—and flattening in the opposite direction. Some examples of experimental data which give this distorted yield surface shape are given in Figs. 6.8–6.13. Although the terminology has been evolving and may vary among the authors, nowadays, this phenomenon is commonly referred to as the *directional distortional hardening (DDH)*. The word "directional" was added to distinguish from cases of simple *distortional hardening*, where distortion changes only the ratio of elliptical axes while maintaining the elliptical shape. The term DDH was firstly coined in Feigenbaum and Dafalias [1]. Distortional hardening is usually observed when a relatively coarser definition of yield is used, while the DDH has been observed when a more sensitive definition of yield is used.

Essentially, DDH is a manifestation of a form of deformation-induced anisotropy, as such it is an important part of modeling the cyclic behavior of materials, including ratcheting, which is the accumulation of plastic strain during cyclic plastic loading. In particular, DDH is often associated with texture development in the microstructure as seen in Dafalias [2] and Feigenbaum and Dafalias [3]. One key reason that DDH is expected to be so important to modeling cyclic plasticity is the associative flow rule, which is typically used for metals and assumes that the normal to the yield surface is the direction of the plastic strain increment. With the associative flow rule, the distorted yield surface shape not only identifies the point at which yield occurs, but the distorted shape also gives rise to the direction of the plastic strain increment. During

Cyclic Plasticity of Metals. https://doi.org/10.1016/B978-0-12-819293-1.00016-4

LaTeX class: roostaei, 2021/05/25 10:02:47 roostaei driver • file: roostaei06.tex (Renata) • Prn: 2021/07/12;14:50:03 • p. 1
pro: ROOSTAEI • model: a03 • color: 1c • ref-style: Numbered (Style 1) • lang: en-US • docsubty: CHP •

B978-0-12-819293-1.00016-4, 00006

cyclic loading, inaccuracies in the direction of the plastic strain increment accumulate and lead to poor predictions over many cycles. To avoid this error accumulation, many researchers have begun considering DDH as a modeling tool which may improve predictions during cyclic plastic loading. According to Bari and Hassan [4] "the best option to achieve a robust model for ratcheting simulations seems to be the incorporation of yield surface shape change."

In this chapter, the state-of-the-art of DDH is explored and expanded. This chapter covers experimental evidence of DDH, development of experimental methods for investigation of yield surface shape and its evolution, early attempts in modeling, models involving higher-order tensors, a new model of DDH, and using DDH to predict cyclic plasticity. The models and experiments in this chapter are generally limited to small strain, rate-independent, room temperature metal plasticity, mainly steels and aluminum alloys. While there are models and experiments for yield surface distortion that exceed these boundaries, e.g., Feigenbaum and Dafalias [3] consider large deformations, and Ishikawa [5] and Dafalias et al. [6] consider rate-dependent plasticity, the majority of prior work on DDH fits within these boundaries, and, as needed, standard procedures can be used to extend the models in this chapter to large deformations and rate-dependent plasticity.

The experimental section 6.2 examines several different procedures and experimental setups for measuring DDH and presents various observed yield surface shapes. This section also addresses some of the complexities related to how yield definition, measurement of Young modulus, materials, and measurement techniques affect the yield surface shape.

In the modeling part of this chapter (Section 6.3), several complex mathematical models of DDH that have been introduced in the last decades are reviewed, and a new segmented (geometry-based) model for DDH is introduced. The historical overview includes several different approaches and models ranging in complexity from those that add only a constant term to a typical von Mises yield function, to those that add a 4th or 6th order tensor to the yield function or to those that can simulate multiple apexes or directions of the yield surface distortion. The new yield function presented in this chapter is defined by arc segments, so that the shape of the yield surface can be well controlled and adjusted to accurately match experimentally found YS shapes.

The new model is used to predict yield surface shape and biaxial ratcheting in Section 6.4. While there are theoretical reasons to believe that DDH may be important to accurately predict cyclic plastic loading, at this point there is still no conclusive evidence for or against DDH as a necessary modeling feature and DDH is not generally used in applications. One of the questions that we attempt to address in Section 6.4 is to what extent, if at all, DDH improves ratcheting predictions. By directly comparing ratcheting results using models with and without DDH, the role of yield surface distortion in predicting strain accumulation during cyclic loading can be analyzed.

Finally, in Section 6.5, important conclusions about how yield surface distortion affects cyclic loading predictions are made. In this section future work is discussed, including, how DDH can be used in applications, how DDH models can be enhanced, and how cyclic plasticity predictions can be improved.

ROOSTAEI, 978-0-12-819293-1

LaTeX class: roostaei, 2021/05/25 10:02:47 roostaei driver • file: roostaei06.tex (Renata) • Prn: 2021/07/12;14:50:03 • p. 2
pro: ROOSTAEI • model: a03 • color: 1c • ref-style: Numbered (Style 1) • lang: en-US • docsubty: CHP •

B978-0-12-819293-1.00016-4, 00006

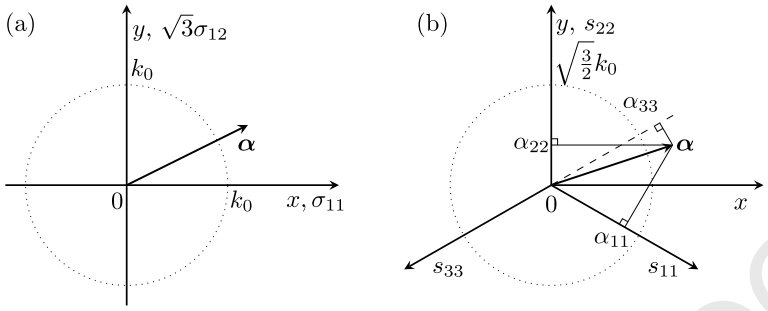

Figure 6.1 Two ways of visualizing phenomena in stress space.

6.1.1 Observing phenomena in stress space

As this chapter focuses on the shape of the yield surface, it is important that the space of visualization be well defined from the start. The two most convenient forms of visualization are presented here in Fig. 6.1 as σ_{11}–σ_{12} space for experiments involving tubular specimens under tension and torsion, and an isometric view of the deviatoric stress plane s_{11}–s_{22}–s_{33} for experiments with tubular specimens under tension and internal pressure inducing the so-called hoop stress. Both diagrams are supplemented with x, y coordinates to help with plotting tensors or fields of various scalar variables.

6.1.1.1 The tension–shear diagram

Due to scaling of the shear dimension, see Fig. 6.1(a), the initial von Mises yield surface is spherical and intersects both axes at the nominal value of k_0. This is favorable as it does not interfere with the expected shape of distortion, but rather makes the evolution of the distortion quite clear to see since the initial YS shape is spherical.

In order to visualize backstress in this space, it is convenient to add fictitious volumetric part to a plotted deviatoric tensor $\boldsymbol{\alpha}$, so that

$$[x, y] = \left[\tfrac{3}{2}\alpha_{11}, \sqrt{3}\alpha_{12}\right]. \tag{6.1}$$

To visualize this situation in an analogous ε_{11}–ε_{12} strain diagram while maintaining σ_{11}–σ_{12} plane stress, a plastic strain tensor $\boldsymbol{\varepsilon}^{\mathrm{p}}$ has to be known. To plot the yield function, coordinates must be defined first as

$$[x, y] = \left[\varepsilon_{11}, \frac{\sqrt{3}}{1+\nu}\varepsilon_{12}\right], \tag{6.2}$$

then the projected stress space for the yield function can be defined as

$$[\sigma_{11}, \sigma_{12}] = E\left[x - \varepsilon^{\mathrm{p}}_{11}, \frac{y}{\sqrt{3}} - \frac{\varepsilon^{\mathrm{p}}_{12}}{1+\nu}\right], \tag{6.3}$$

ROOSTAEI, 978-0-12-819293-1

B978-0-12-819293-1.00016-4, 00006

where linear elasticity has been assumed, E is the Young modulus, ν is the Poisson ratio. With this scaling, the projection of a von Mises sphere is circular and therefore equal in all directions. The scaling in Eqs. (6.2)–(6.3) differs from the widely used $(\varepsilon, \gamma/\sqrt{3})$, which stems from the definition of equivalent strain, and does not result in a circular von Mises yield surface.

6.1.1.2 Deviatoric stress plane in isometric view

Using the deviatoric stress plane with an isometric view, the axes are not orthogonal but rather are 120° degrees apart. We define the following convenient coordinate system:

$$[x,\ y] = \left[\sqrt{\tfrac{1}{3}}\,(s_{11} - s_{33})\,,\ s_{22}\right] = \left[\sqrt{\tfrac{1}{3}}\,(\sigma_{11} - \sigma_{33})\,,\ \tfrac{2}{3}\sigma_{22} - \tfrac{1}{3}\,(\sigma_{11} + \sigma_{33})\right], \tag{6.4}$$

which is orthogonal, and can be inverted to give

$$[s_{11},\ s_{22},\ s_{33}] = \left[\sqrt{\tfrac{3}{4}}x - \tfrac{1}{2}y,\ y,\ -\sqrt{\tfrac{3}{4}}x - \tfrac{1}{2}y\right]. \tag{6.5}$$

For a biaxial σ_{11}–σ_{22} stress problem projected to the deviatoric strain space ε'_{11}–ε'_{22}–ε'_{33} where $\varepsilon'_{ij} = \varepsilon_{ij} - \frac{1}{3}\delta_{ij}\varepsilon_{kk}$, the coordinate system is defined by

$$[x,\ y] = \left[\sqrt{\tfrac{1}{3}}\left(\varepsilon'_{11} - \varepsilon'_{33}\right),\ \varepsilon'_{22}\right] = \left[\sqrt{\tfrac{1}{3}}\left(\frac{s_{11} - s_{33}}{2G} + \varepsilon^{\mathrm{p}}_{11} - \varepsilon^{\mathrm{p}}_{33}\right),\ \frac{s_{22}}{2G} + \varepsilon^{\mathrm{p}}_{22}\right]. \tag{6.6}$$

Accordingly, the initial von Mises sphere intersects any of the axes at

$$\varepsilon'_{ii} = \frac{\sigma_{\mathrm{Y}}}{3G}. \tag{6.7}$$

6.2 Experimental measurement of yield surface distortion

The present section provides an overview of experimental investigations into yield surface shape and distortion. In most of the literature, the yield surface is detected experimentally by subjecting thin-walled tubular specimens to combined loading in two or three directions, however, a few researchers used other methods to determine the yield surface shape. All of these methods are discussed in Sections 6.2.1 and 6.2.2, and the advantages/disadvantages of each test set-up are considered. Later, in Sections 6.2.3 and 6.2.4 some details and challenges in current experimental methods concerning the yield point definition and elastic moduli influence are discussed. Section 6.2.5 presents several sets of experimental results by different authors. The yield

ROOSTAEI, 978-0-12-819293-1

LaTeX class: roostaei, 2021/05/25 10:02:47 roostaei driver • file: roostaei06.tex (Renata) • Prn: 2021/07/12;14:50:03 • p. 4
pro: ROOSTAEI • model: a03 • color: 1c • ref-style: Numbered (Style 1) • lang: en-US • docsubty: CHP •

B978-0-12-819293-1.00016-4, 00006

surfaces shown in this subsection emphasize how distortion affects various metals, e.g., steels, pure aluminum, aluminum alloys, copper, brass, and titanium. Finally, this section concludes with a critical look at the state-of-the-art in experimental methods to determine the yield surface shape, including challenges that have been overcome, inaccuracies in the data that have been generally accepted, and results that reveal some new aspects of distortional hardening.

6.2.1 Development of experimental research

Some of the first experiments that identified distortion of the yield surface due to plastic straining of metals were performed on sheet metal. In these experiments, the yield surface was determined by testing of strips of metals cut off from the cold-rolled sheets at different angles to the rolling direction, e.g., Körber and Hoff [7], Cook [8], and Klinglert and Sachs [9]. Note that the first model capable of capturing the yield strength anisotropy—which might be considered a particular yield surface distortion—was published by Hill [10]. However, the first experiments where distortion was induced by plastic straining of specimens directly on testing devices during the experiment are from the late 1950s and early 1960s, e.g., Naghdi et al. [11], McComb [12], Ivey [13], Szczepiński [14], and Mair and Pugh [15].

From the beginning in 1950s, the experimental work on yield surface shape was mainly influenced by the mathematical theory of plasticity by Batdorf and Budiansky [16]. The theory predicted the existence of corners in subsequent yield surfaces, and researchers dedicated an enormous effort to develop and enhance experimental methods to validate this theory. Some contemporary references show disagreement in experimental results, findings, and conclusions by different authors. For instance, Hecker [17] referred to 7 original papers that support the existence of corners, and to 7 original papers that reject their existence. Hence, a contradiction and uncertainty in experimental results and subsequent conclusions may be seen, which suggests that experimental analysis of distortion is intricate and requires sophisticated and consistent methods to be used. A detailed summary on the yield surface corner investigation may be seen in Michno and Findley [18] and Kuwabara [19]. Note that current phenomenological plasticity models mainly do not support the existence of corners in the yield surfaces.

Phillips et al. [20] and Phillips and Tang [21] studied distortion of yield surfaces at ambient and elevated temperatures, namely at 21 °C, 66 °C, 108 °C, and 152 °C. They experimentally proved that the decrease of yield strength due to increasing temperature—which is well known from uniaxial testing—holds under combined axial load and torque. In particular, original and subsequent yield surfaces depicted in $\sigma - \sqrt{3}\tau$ space shrink due to temperature elevation. Note that the authors used very fine definition of yielding by the proportional limit (see Section 6.2.3), and they achieved remarkably consistent results.

In general, distortion of yield surfaces in experimental research is usually induced by straining to a prescribed total strain level rather than a prescribed stress level, as shown in Fig. 6.2. On the other hand, subsequent detection of the shape of distorted yield surface is usually done by a probe in the stress space, as indicated in Fig. 6.3.

ROOSTAEI, 978-0-12-819293-1

LaTeX class: roostaei, 2021/05/25 10:02:47 roostaei driver • file: roostaei06.tex (Renata) • Prn: 2021/07/12;14:50:03 • p. 5
pro: ROOSTAEI • model: a03 • color: 1c • ref-style: Numbered (Style 1) • lang: en-US • docsubty: CHP •

B978-0-12-819293-1.00016-4, 00006

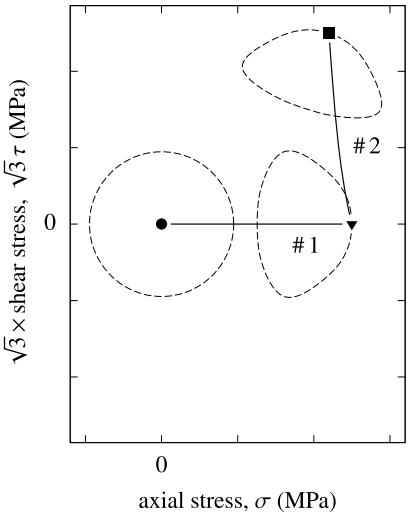

Figure 6.2 Example of loading paths to distort yield surfaces: (●) no prestrain, (▼) prestrain to 2 % of total axial strain, and (■) subsequent prestrain to 1 % of total shear strain.

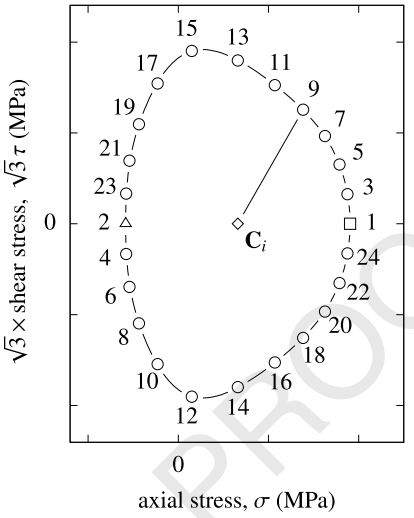

Figure 6.3 Example of probing paths to detect distorted yield surface: (□) 1st probing point, (△) 2nd probing point, (◇) center point, (○) subsequent probing points, and (–) probing path.

Hence the probe is a loading case to determine a particular yield surface point with negligible influence on the yield surface evolution.

Phillips and Lu [22] employed both the stress and strain paths to detect distortion. To measure strain, they used rosette strain gages with the sensitivity below 1 $\mu\varepsilon$ ($1\,\mu\varepsilon = 10^{-6}$ m/m). Besides the detection of yield surface distortion, Phillips and Lu [22] also determined plastic strain increments at yielding. This is a crucial experimental achievement which allows validation of flow rules inherent to plasticity models.

A remarkable experimental work was contributed by Wu and Yeh [23]. In their paper, authors discussed in detail factors affecting yield surfaces detection, e.g., the elastic moduli and zero offset strains variations, strain domain range, probing paths pattern, and the probing strain rate. To suppress the effect of plastic strain accumulation, they followed specific pattern of probing paths with directions perpendicular to the loading direction and alternating orientations between subsequent probes. As experimental data is provided in numerical form, it is convenient for plasticity models validation. Note that the offset strain threshold of 5 $\mu\varepsilon$ was used to define yielding.

The experimental work mentioned thus far was mainly focused on small prestrains. The reason is that even small prestrains cause substantial distortion of yield surfaces in the stress space, as can be seen in Figs. 6.8–6.13. Contrarily, finite strain approach brings in many challenges to the experimental plasticity, including more general stress and strain measures, geometrical instability of specimens, range limits of instruments, etc. Wu et al. [24] addressed an influence of large prestrains on yield surfaces distortion. In their experiments, they prestrained specimens up to 20% of total axial strain and to 20% of total shear strain. To measure stress, they used three different stress

ROOSTAEI, 978-0-12-819293-1

LaTeX class: roostaei, 2021/05/25 10:02:47 roostaei driver • file: roostaei06.tex (Renata) • Prn: 2021/07/12;14:50:03 • p. 6
pro: ROOSTAEI • model: a03 • color: 1c • ref-style: Numbered (Style 1) • lang: en-US • docsubty: CHP •

B978-0-12-819293-1.00016-4, 00006

measures, namely the *Cauchy stress*, the *first Piola–Kirchhoff stress*, and the *second Piola–Kirchhoff stress*. The offset strain threshold of $5\,\mu\varepsilon$ was used to distinguish yielding.

Older testing machines had limited capabilities for applying axial and torque loading simultaneously. Therefore, when the probe under combined axial load and torque was addressed, experimenters preferred to split such probe into two or more steps. Then, each step was done either by increasing axial load or torque, i.e., probes were split into horizontal and vertical lines in the axial stress–shear stress space. Since modern testing systems allow simultaneous loading, yield surfaces detection is usually conducted by a sequence of radial probes, as shown in Fig. 6.3. Some first experiments with radial probes were carried out by Ishikawa [5], who also pointed out that the identification of respective center point—denoted by $\mathbf{C}_i$ in Fig. 6.3—may affect the shape of detected surface. The offset strain used for the yielding definition was $50\,\mu\varepsilon$.

Sung et al. [25] loaded specimens by combined axial load, torque, and internal pressure. Moreover, they employed an autonomous testing system controlled by a script. For many reasons, this might be considered a state-of-the-art approach. First, the script control of this experimental setup allows to design entire experiment in advance and, consequently, run the experiment autonomously, i.e., with no need of intervention from the researcher(s). This considerably increases the repeatability of the results. Further, current testing systems are capable of feedback control and real-time data evaluation in high-level programming languages, e.g., C# and Python. This is crucial when single specimen is used to carry out many probes, since probing path may be terminated as soon as the yield condition is met, thereby avoiding excessive accumulation of plastic strain. More details are made available in Section 6.2.3. Clearly, the script control brings much advantage known from programming, including portability, modifiability, and modularity, especially when the control script is well designed, structured, and parametrized. Sung et al. [25] subjected acquired experimental data to statistical analysis and defined yielding by the offset strain threshold of $12.5\,\mu\varepsilon$.

While the previously mentioned experiments all support convexity of distorted yield surfaces—see Figs. 6.8–6.13—some recent experiments by Liu et al. [26] suggest that the loss of convexity might occur. The authors distinguished between the single- and multi-sample methods. The single-sample method employs a single specimen to determine entire yield surface, i.e., multiple probes are used per one specimen (sample). On the other hand, the multi-sample method requires multiple specimens to obtain one yield surface, since each probe requires a new specimen. These authors reported mutual influence of subsequent probes when the single-sample method was used, and they attributed this observation to the plastic strain accumulation. Moreover, when the multiple-sample method was used together with a fine offset strain definition as of $20\,\mu\varepsilon$, the authors observed clear loss of convexity in the rear part of distorted yield surfaces, i.e., in the part opposite to the prestraining direction. Finally, it is worth mentioning that the multi-sample method does not necessarily expend one specimen to detect one point of the yield surface. Instead, the probe may go on beyond the first yield point in the original direction and subsequent yield points that correspond to

ROOSTAEI, 978-0-12-819293-1

LaTeX class: roostaei, 2021/05/25 10:02:47 roostaei driver • file: roostaei06.tex (Renata) • Prn: 2021/07/12;14:50:03 • p. 7
pro: ROOSTAEI • model: a03 • color: 1c • ref-style: Numbered (Style 1) • lang: en-US • docsubty: CHP •

B978-0-12-819293-1.00016-4, 00006

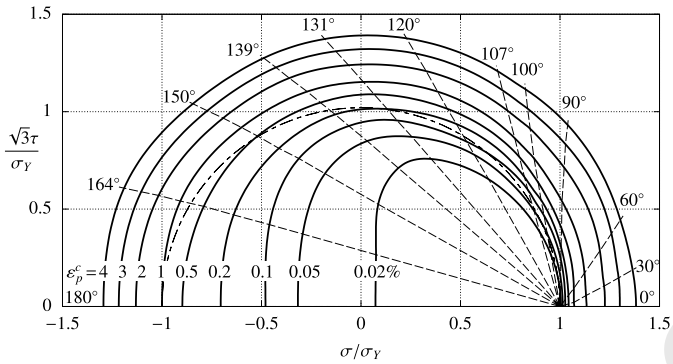

Figure 6.4 An example of experimental results by Ohashi et al. [27]. Probes are not terminated once the first yield surface is reached, but they go on to considerable strain to uncover further information.

higher strain offsets may be determined, as shown by Ohashi et al. [27] on mild steel and in Fig. 6.4.

6.2.2 Experimental methods to detect yield surfaces distortion

In general, there are two main challenges concerning experimental methods used to detect yield surfaces distortion. The first challenge is to achieve uniform stress state in the material. This is crucial since the uniform stress state induces uniform strain in the bulk, which makes it significantly easier to measure the strain in the material. The second main challenge is to load in various different probing directions relative to the loading direction of prestraining, i.e., relative to the loading that induced distortion of the yield surface, in order to fully detect the yield surface shape, and not just a single yield point. Not only is it necessary to probe in several different directions, but when a single specimen is to be used, the load used for probing must be stopped at the exact onset of yielding and unloaded in order to avoid changing the state of the material due to additional, undesired, plastic loading during probing. In addition to these challenges, researchers must also maintain the stability of the specimen, avoiding dynamic effects, and making certain that the signal to noise ratio is high enough to have confidence in the results. Several experimental techniques have been developed to detect yield surface distortion after prestraining. The most frequently employed ones are described below. Also, to provide an overview of experimental research, some notable experiments are listed in Table 6.1.

For more details, the reader is referred to Guest [53] (this pioneering work includes an overview of different methods), Hill [54], Ikegami [55], Ikegami [56], Michno and Findley [18], Hecker [57], Ikegami [58] (this work has a summary for different materials as in Table 6.1), Bell [59], Phillips [60], Szczepiński [61], Stout and Kocks [62], McDowell [63], and Kuwabara [19]. Note that some of these references did not aim at characterizing plasticity and yield surfaces detection, however, as they employed testing setups or methodology suitable to detect yield surfaces, they are included.

ROOSTAEI, 978-0-12-819293-1

LaTeX class: roostaei, 2021/05/25 10:02:47 roostaei driver • file: roostaei06.tex (Renata) • Prn: 2021/07/12;14:50:04 • p. 8
pro: ROOSTAEI • model: a03 • color: 1c • ref-style: Numbered (Style 1) • lang: en-US • docsubty: CHP •

B978-0-12-819293-1.00016-4, 00006

Table 6.1 An overview of experimental works on the detection of distorted yield surfaces.

Authors	Material	Experimental method	Specimen's geometry	Offset strain	Yield surface shape
Naghdi et al. [11]	AA 24S-T-4	A–T	22.9/1.9/12.0	propor.	DDH
McComb [12]	AA 2014-T4	A–T	114.3/4.0/28.8	propor.	DDH
Ivey [13]	5 × AA	A–T	27.4/1.0/27.0	propor.	DDH
Phillips and Gray [28]	AL 2S-O	A–T	21.6/1.3/17	–	corner
Szczepinski [14]	AA	A	strips	100 με	DDH
Mair and Pugh [15]	copper	A–T	27.4/1.0/27.0	100 με	DDH
Theoc. and Hazell [29]	AL 6061-T 651	bending	plates	–	corner
Szczep. and Miast. [30]	AA PA-3	A	strips	100 με	DDH
Will. and Svens. [31]	AL 1100-F	A–T	27.9/1.3/22.0	20 με	DDH
Will. and Svens. [32]	AA 1100-F	A–T	27.9/1.3/22.0	20 με	DDH
Hecker [17]	AL 1100, OFHC copper	A–P	27.1/1.0/26.6	5 με	DDH
Phillips et al. [20]	AL	A–T	54.9/1.3/43.3	5 με	DDH
Phillips and Tang [21]	AL 1000-0	A–T	54.9/1.3/43.3	3 με	DDH
Shirat. et al. [33]	brass	A–T–P	23.0/1.5/15.3	200 με	DDH
Michno and Findley [34]	ST SAE 1017	A–T	25.4/1.5/16.7	10 με	DDH
Ohashi et al. [27]	mild ST	A–T	21.0/1.0/21.0	200 με	DDH
Shirat. et al. [35]	AA 17S	A–T	23.0/1.5/15.3	200 με	DDH
Ascione et al. [36]	AL	A	strips	10 με	distortion
Ellis and Robinson [37]	ST 316	A–T	–	10 με	DDH
Troshch. and Kul'ch. [38]	ST 40Kh	A–T	27.0/1.0/27.0	2,000 με	DDH
Phillips and Lu [22]	AL 1100-0	A–T	54.9/1.3/43.3	≈14 με	DDH
Phillips and Das [39]	AL 1100-0, brass	A–T–P	45.2/1.1/42.4	2 με	DDH
Stout et al. [40]	AL 1100	A–T	12.1/1.3/9.5	5 με	DDH
Helling et al. [41]	AL, AA, 70:30 brass	A–T	11.6/0.34/34.1, 11.2/0.25/44.0	5 με	DDH
Wu et al. [42]	ST 304	A–T	16.1/1.7/9.5	≈20 με	–
Cheng and Krempl [43]	5005 Al/Mg	A–T	18.6/1.8/10.5	100 με	DDH
Wu and Yeh [23]	ST AISI 304	A–T	15.2/1.3/12.0	5 με	DDH
Khan and Wang [44]	OFHC copper	A–T	11.4/1.0/12.0	200 με	DDH
Boucher et al. [45]	AA 2024, ST	A–T	25.4/1.5/16.6	40 με	DDH
Wu et al. [24]	ST AISI 304	A–T	15.2/1.3/12.0	5 με	DDH
Dietrich and Kowal. [46]	M1E copper	A–T	17.5/0.8/23.3	100 με	distortion
Ishikawa [5]	ST SUS 304	A–T	23.0/1.5/15.3	50 με	distortion
Lissenden et al. [47]	ST 316	A–T	26.0/2.0/13.0	propor.	DDH
Gil et al. [48]	Inconel 718	A–T	21.0/2.6/8.1	30 με	DDH
Dannemeyer [49]	ST S235, S355, AA AlMg3	A–T A–T	28.0/1.5/18.7 28.0/2.0/14.0	30 με	DDH
Brown et al. [50]	AL 1100	A–T	56.3/2.5/22.2	5 με	DDH
Khan et al. [51]	AL 6061-T6511	A–T	15.5/2.8/11.0	10 με	DDH
Sung et al. [25]	AA 6061	A–T–P	25.0/1.5/16.7	12.5 με	DDH
Hu et al. [52]	ST 45	A–T	12.5/1.0/12.5	2,000 με	DDH

The entries in the "Specimen's geometry" column refer to "outer diameter (mm)/wall thickness (mm)/respective ratio". The entries in the "Offset Strain" column subject to testing method, but usually refer to von Mises effective strain, axial strain, or shear strain offsets. Abbreviations are as follows: AA aluminum alloy, AL pure aluminum, ST steel, A axial load, T torque, P internal pressurizing; $1\,\mu\varepsilon = 10^{-6}\,\mathrm{m/m}$.

ROOSTAEI, 978-0-12-819293-1

B978-0-12-819293-1.00016-4, 00006

Axial load–internal pressure

Lode [64], Hu and Bratt [65], Hecker [17], and Khan et al. [66], among other authors, carried out experiments on thin-walled tubular specimens loaded by combined axial load and internal pressure. In general, this kind of loading results in triaxial stress state with the stress gradient in the radial direction of the specimen. However, when the wall thickness to specimen's diameter ratio is small enough—usually in the range of 1:15 to 1:30—the radial stress may be neglected and biaxial stress state is well approximated.

Clearly, due to symmetry, there are no shear stresses present in the planes given by axial, tangential, and radial normal directions. Therefore, the axial stress and hoop stress in axial and tangential directions, respectively, act as the principal stresses. Moreover, as directions of principal stresses are independent of load, principal axes remain aligned with specimen's axes, which is a distinguishing feature of this testing method. In particular, this attribute should be reflected in the design of experiments on anisotropic materials. More details on anisotropy are available in Rotvel [67], who used this method in biaxial fatigue tests. Also, it is worth mentioning that internal pressurizing induces tensile hoop stress only, and, therefore, Rotvel [67] employed external pressurizing to achieve compression as well.

Axial load–torque

The most frequently used method employs combined axial load and torque applied to thin-walled tubular specimens. It is reported by Taylor and Quinney [68], Schmidt [69], Morrison [70], Naghdi et al. [71], Naghdi et al. [11], McComb [12], Ivey [13], Phillips and Gray [28], Bertsch and Findley [72], Paul et al. [73], Mair and Pugh [15], Wu and Yeh [23], and Dannemeyer [49], among other authors. Regarding the design of specimens, like in the previous method, the wall thickness to diameter ratio is required to be small enough in order to limit the variation of shear stress across the wall thickness, therefore keeping the stress uniform. The combined load is commonly achieved by biaxial testing systems, and strains are usually measured by biaxial extensometers or strain gage rosettes. The biaxial stress state is achieved, though principal axes do not remain fixed, but rather rotate as the axial load and torque vary. This is in contrast to the method of combined axial load and internal pressure described above. The variation of principal axes may be limiting when anisotropic material is being examined, as reported by Rotvel [67].

Axial load–torque–internal pressure

The most general testing method in terms of independent loading channels combines both methods described above. Thin-walled tubular specimens are loaded by a combination of axial load, torque, and internal pressure. This method was employed by several authors, e.g., Shiratori et al. [33], Phillips and Das [39], and Sung et al. [25], and allows achieving biaxial stress state by a variation of three independent components of the stress tensor that match the axial, shear, and hoop stress.

ROOSTAEI, 978-0-12-819293-1

LaTeX class: roostaei, 2021/05/25 10:02:47 roostaei driver • file: roostaei06.tex (Renata) • Prn: 2021/07/12;14:50:04 • p. 10
pro: ROOSTAEI • model: a03 • color: 1c • ref-style: Numbered (Style 1) • lang: en-US • docsubty: CHP •

B978-0-12-819293-1.00016-4, 00006

In general, experimental methods of yield surfaces detection based on thin-walled tubular specimens testing are time consuming, since they require many probing trajectories to represent yield surface with sufficient number of yield points. Sung et al. [25] developed a script-controlled testing setup enabling fully automated testing, which allows for reducing testing duration. From their results, they concluded that initial yield surfaces in three-dimensional stress space may not fully conform to von Mises condition due to initial anisotropy of material. Besides, they observed some complex hardening effects manifested by rotation of yield surfaces.

Uniaxial testing of strips

The simplest method to detect distorted yield surfaces is based on tensile testing of specimens cut off from a single sheet of prestrained material. This method was used by several authors, e.g., Körber and Hoff [7], Cook [8], Klinglert and Sachs [9], Szczepiński [14], and Ascione et al. [36]. First, the sheet of metal is prestrained, and strips are cut off at different angles with respect to the direction of prestraining. Then, the strips undergo tensile testing, and particular yield strength represents the size of distorted yield surface in respective direction.

This method has several advantages. First, specimens' geometry is quite simple, which reduces manufacturing costs. Next, specimens are subjected to tensile tests, which is a common experimental procedure. Also, multiple tests in a particular direction are possible depending on number of specimens cut off in the same direction, which allows for precision to be evaluated.

On the other hand, a high-capacity testing system is required to prestrain original sheet. Moreover, the sheet must be completely unloaded to cut off the strips, which may be constraining in respect to the other methods. This is due to the fact that distorted yield surfaces may drift away from the origin of the stress space, as indicated by results from combined axial load and torque experiments shown in Figs. 6.8 and 6.11. As the specimen must be completely unloaded when the method of uniaxial testing of strips is used, observation of this phenomenon is beyond capability of the method. Also, as it is challenging to subject the sheet to shear prestrain, the method suffers from the limited number of potential prestraining modes.

Biaxial testing of sheets

This approach is motivated mainly by modeling of sheet metal forming. It covers several different methods being extensively described by Shiratori and Ikegami [74] and Kuwabara [19], e.g., biaxial tensile testing on cross-shaped specimens, compressive testing of blocks of material, and biaxial compressive testing on adhesive bonded sheet laminate specimens. In general, these methods require special testing systems capable of biaxial loading. Although the methods are expected to utilize simpler geometry of specimens than in the case of tubular specimens, the manufacturing of fine cross-shaped specimens may be challenging. Also, the stress state achieved under biaxial compressive testing is influenced by friction between the clamping and specimen in the same manner as uniaxial compressive tests.

ROOSTAEI, 978-0-12-819293-1

LaTeX class: roostaei, 2021/05/25 10:02:47 roostaei driver • file: roostaei06.tex (Renata) • Prn: 2021/07/12;14:50:04 • p. 11
pro: ROOSTAEI • model: a03 • color: 1c • ref-style: Numbered (Style 1) • lang: en-US • docsubty: CHP •

B978-0-12-819293-1.00016-4, 00006

Plate bending method

Theocaris and Hazell [29] used a method based on the measurement of deflections in square- and rhomboid-shaped plates subjected to bending. The plates were illuminated by a collimated light beam forming an oblique moiré pattern on the surface of plates. From the moiré pattern, the relative deflection of plates might be computed. The authors developed an advanced experimental method that employs several sophisticated techniques. To relate the stress and displacement fields, they used the theory of plates. To achieve required stress states, they used square- and rhomboid-shaped specimens and explored several configurations for loads and supports. Some stress states were even achieved virtually by making use of the superposition of two real states. The main disadvantage of this method is that it does not allow one to determine absolute values of yield stresses of tested material, but rather a relative shape of yield surfaces in the two-dimensional space of bending moments.

6.2.3 Yield definition

The yield point is the point on stress–strain curve where deformation of strained material transits from purely elastic to elasto-plastic one. In theory, the above definition is straightforward and implies that the yield point can be set as the point where permanent deformation during loading of material is first observed. From experimental point of view, however, this approach has several challenges that make this definition cumbersome to implement. Moreover, the experimentally determined yield surface shape can be quite sensitive to how this definition is implemented.

The reason for the experimental challenge is because most experimental methods use the direct measurement of deformation and strain. In particular, the elongation and strain are usually measured by extensometers, strain gages, or by video extensometers. Such techniques determine the total strain, but they are not capable of measuring elastic and plastic parts of total strain separately. To overcome this issue, a series of loading and unloading steps would be necessary together with regular measurements of total strain in each unloaded configuration. This would make yield point determination quite time consuming and imprecise, and would subject the specimen to cyclic loading. Besides, determining the onset of plastic strain would require measurement of the residual strain after unload, which is always strongly affected by sensitivity and accuracy of the measurement device. Thus, researchers attempted to establish methods to determine yield point which avoids subsequent loading steps, thus preserving or approximating the meaning of yield as the onset of permanent strain. Possible yield point definitions employed by different authors are shown in Fig. 6.5.

Many authors defined yielding by the *proportionality limit*, e.g., McComb [12], Ivey [13], Phillips et al. [20], and Phillips and Tang [21]. In Fig. 6.5, this definition is represented by the point A and shows where the stress–strain curve first begins to be nonlinear. Although this approach seems to be quite simple, it has two main drawbacks. First, the method requires material to exhibit linear elastic behavior, which makes this method inappropriate for materials with nonlinear behavior in the elastic domain. Moreover, no universal quantification of linearity deviation is given, which

ROOSTAEI, 978-0-12-819293-1

LaTeX class: roostaei, 2021/05/25 10:02:47 roostaei driver • file: roostaei06.tex (Renata) • Prn: 2021/07/12;14:50:04 • p. 12
pro: ROOSTAEI • model: a03 • color: 1c • ref-style: Numbered (Style 1) • lang: en-US • docsubty: CHP •

B978-0-12-819293-1.00016-4, 00006

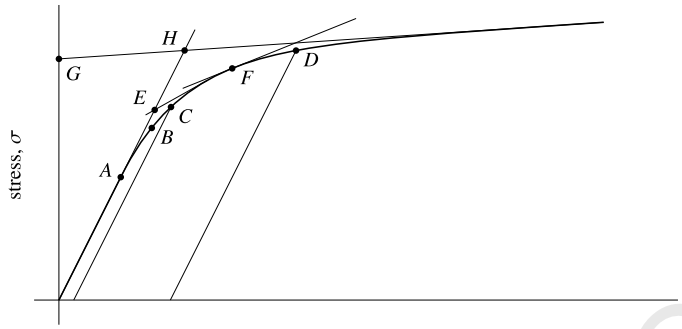

Figure 6.5 Various definitions of yield point used in experiments of yield surfaces detection: A, proportionality limit; B, elastic limit; C, small offset strain; D, 0.2% offset strain; E, backward extrapolation of onset of elasto-plastic part; F, elastic modulus fraction; G, elasto-plastic part extrapolation back to the zero total strain; and H, elasto-plastic part extrapolation back to the elastic line.

led authors to adopt the lowest deviation from linearity capable of detecting by their experimental setup. Due to this, the yield point detection strongly depends on the sensitivity of instruments, the method often gives scattered data, and plastic anisotropy of material is pronounced. Some more information on the influence of measurement sensitivity may be seen in Hecker [57].

As some materials may exhibit pure elastic deformation of nonlinear type beyond the proportionality limit, it is reasonable to define the yield point by the *elastic limit*, i.e., point B shown in Fig. 6.5. The elastic limit B is the highest stress that does not cause any permanent deformation. Thus, the plastic deformation begins at the onset of permanent deformation. Despite the clear physical interpretation, this definition suffers from problems described above for the proportionality limit. Namely, this method provides no general threshold to distinguish between the negligible residual strain and the permanent strain. Further, repeated unloading is needed to determine the permanent strain.

The yield surface detection experiments mostly employ the *proof stress* definition of the yield point, e.g., Szczepiński [14], Helling et al. [41], and Wu and Yeh [23]. In Fig. 6.5, the respective yield point is denoted by C. The crucial component in this definition is the offset strain which reads

$$\varepsilon_{\text{off}} = \varepsilon^{\text{tot}} - \frac{\sigma}{E}\,, \tag{6.8}$$

where ε^{tot} is the total strain read from extensometer or similar device, σ is the stress measured by load cell, and E is the Young modulus of material. Clearly, the offset strain in Eq. (6.8) represents the difference between the total strain and the elastic strain, i.e., the plastic strain. The offset strain is being evaluated during the loading and fluctuates around zero as long as the stress state remains in the elastic domain. Beyond the elastic domain, rapid increase in value occurs, and the yield point is reached when the offset strain achieves a prescribed threshold. This threshold varies among authors,

ROOSTAEI, 978-0-12-819293-1

LaTeX class: roostaei, 2021/05/25 10:02:47 roostaei driver • file: roostaei06.tex (Renata) • Prn: 2021/07/12;14:50:04 • p. 13
pro: ROOSTAEI • model: a03 • color: 1c • ref-style: Numbered (Style 1) • lang: en-US • docsubty: CHP •

B978-0-12-819293-1.00016-4, 00006

but usually falls in the range of 10–200 $\mu\varepsilon$. Early experimental data often use higher thresholds, but there are many exceptions. Note that in engineering, the proof stress definition of the yield point relies on standardized offset strain threshold of $0.2\% = 2000\,\mu\varepsilon$. This standardized engineering definition is shown as point D in Fig. 6.5. The main benefit of the method described is that no repetitive unloading steps are required. On the other hand, the assumption that material obeys Hooke law may be limiting for some materials. Even if a material does obey Hooke law, when a small offset strain is used, it is imperative to have highly accurate measurements of the modulus as small changes to E in Eq. (6.8) can dramatically change ε_{off}. This will be discussed further in Section 6.2.4.

Another approach to the yield point definition was established by Phillips et al. [20]. The authors were tracing first deviation of the stress–strain curve from Hooke law such as in the proportionality limit definition. As soon as more than two subsequent readings deviated from linearity and declined to the same side, the onset of this deviation was extrapolated back to the elastic line. In Fig. 6.5, this *backward extrapolation* leads to the yield point E. Using this method, they were able to keep the accumulated strain up to $5\,\mu\varepsilon$ and obtained remarkably consistent results, however, using two subsequent readings may lead to inconsistent results if the rate of data collection varies.

Several authors used other approaches to experimentally determine the yield point. Hecker [57] and Ikegami [58] referred to the *elastic modulus fraction*, which is represented by the point F in Fig. 6.5. Taylor and Quinney [68] and Parker and Bassett [75] extrapolated elasto-plastic part of the stress–strain curve back to the zero plastic strain, shown as point G in Fig. 6.5. Mair and Pugh [15] extrapolated elasto-plastic part of the stress–strain curve back to the elastic line, as shown by point H in Fig. 6.5. Note that Fig. 6.5 and the list of presented definitions for yield is not exhaustive. There are various modifications and slight differences among authors, but these represent some of the most commonly used yield definitions.

So far, we have based the definition of yielding on stress–strain curve evaluation. While this curve is inherent to uniaxial loading mode, current methods for yield surface detection mainly employ multiaxial testing. To overcome this issue, authors usually reduced multiaxial stress states into simple stress–strain relation and used the same definitions as shown in Fig. 6.5 and already described in this section.

The simplest method is to restrict yielding observation to a single component of the stress and the total strain tensor, e.g., Ivey [13] and Mair and Pugh [15]. Ivey [13] carried out experiments on thin-walled tubular specimens subjected to combined axial load and torque. To determine the yield surface, the specimen was first prestrained in elastic regime by axial load. Further, the axial load remained fixed, and torque was applied. Thus, the shear stress–shear strain curve could be plotted, and yielding could be evaluated by means of proportionality limit introduced in Fig. 6.5. In general, this method is preferred in former papers and seems to be convenient under non-proportional loading modes, i.e., when particular steps of stress or strain components are applied subsequently rather than simultaneously.

Some authors preferred to evaluate several separate stress–strain curves relating particular stress and strain components, e.g., Phillips et al. [20]. Again, the method-

ROOSTAEI, 978-0-12-819293-1

LaTeX class: roostaei, 2021/05/25 10:02:47 roostaei driver • file: roostaei06.tex (Renata) • Prn: 2021/07/12;14:50:04 • p. 14
pro: ROOSTAEI • model: a03 • color: 1c • ref-style: Numbered (Style 1) • lang: en-US • docsubty: CHP •

B978-0-12-819293-1.00016-4, 00006

ology as in Fig. 6.5, point E, was used to define yielding. However, when several separate stress–strain curves were used, yield was defined as when any of the strains reached the prescribed value for offset strain.

Most recent experiments seek to define yield using multiaxial testing, however, rely on strength theories and *effective plastic strain* definition, e.g., Parker and Bassett [75], Shiratori and Ikegami [74], Wu and Yeh [23], and Sung et al. [25]. The testing methodology by Wu and Yeh [23] will be described in detail as a representative example that includes all crucial aspects of current experimental methods of distorted yield surfaces detection. The authors used thin-walled tubular specimens loaded by combined axial load and torque. Total axial strain ε^{tot} and total shear strain γ^{tot} were measured by strain gage rosettes. Axial stress σ and shear stress τ were determined from loads that were read from load cell. The offset strain ε_{off} was given by von Mises effective plastic strain in the form

$$\varepsilon_{\text{off}} = \sqrt{\left(\varepsilon^{\text{tot}} - \frac{\sigma}{E} - \varepsilon_0\right)^2 + \frac{1}{3}\left(\gamma^{\text{tot}} - \frac{\tau}{G} - \gamma_0\right)^2}, \tag{6.9}$$

where E and G are the Young modulus and shear modulus, respectively, and ε_0 and γ_0 are zero offset strains. Zero offset strains ε_0 and γ_0 are introduced to suppress residual offsets in unloaded configuration. These offsets are determined together with elastic moduli by application of linear regression on experimental data in elastic domain. The multiplier $1/3$ in Eq. (6.9) refers to von Mises effective strain. Thus, Eq. (6.9) replaces Eq. (6.8) under biaxial loading conditions to calculate the difference of total and elastic strains results, which gives the offset plastic strain. To define yielding, Wu and Yeh [23] used the offset strain threshold of $5\,\mu\varepsilon$.

For more information on yielding definition and testing methodology, the reader is referred to Phillips and Tang [21], Hecker [57], Ikegami [58], Wu and Yeh [23], and Sung et al. [25].

6.2.4 Elastic moduli influence

In Section 6.2.2, we have described an experimental method to detect yield surfaces distortion based on investigation of thin-walled tubular specimens subjected to simultaneous axial load and torque. To implement the method, an offset strain formula as in Eq. (6.9) or similar is used together with some small offset strain threshold being prescribed; see Gil et al. [48]. In the equation, four variables ε^{tot}, γ^{tot}, σ, and τ, represent four experimental channels to be read from testing setup. Besides the variables acquired from channels, elastic moduli E and G and zero offset strains ε_0 and γ_0 need to be known to evaluate Eq. (6.9). Here, we should emphasize that accurate determination of these variables is essential, since current experiments employ offset strains threshold of $10\,\mu\varepsilon$, which is about 2 orders of magnitude lower than that commonly used in engineering.

The simplest way to determine elastic moduli is to use values standardized for particular material or measure them apart from the experiment of yield surfaces detection. These approaches, however, considerably decrease accuracy of the offset strain

LaTeX class: roostaei, 2021/05/25 10:02:47 roostaei driver • file: roostaei06.tex (Renata) • Prn: 2021/07/12;14:50:04 • p. 15
pro: ROOSTAEI • model: a03 • color: 1c • ref-style: Numbered (Style 1) • lang: en-US • docsubty: CHP •

B978-0-12-819293-1.00016-4, 00006

evaluation by Eq. (6.9) for many reasons. First, elastic moduli may be affected by heat treatment or manufacturing technology of material, so final properties of material may differ from standardized values. Further, accuracy of elastic moduli measurement depends on the accuracy of the specimen's diameters measurement. The term that represents axial elastic strain in Eq. (6.9) may be written as

$$\varepsilon^{\mathrm{e}} = \frac{\sigma}{E} = \frac{4F}{\pi\left(D^2 - d^2\right)E}, \tag{6.10}$$

where F is the axial load directly measured from the load cell, and D and d are the outer and inner diameters of the tubular specimen, respectively. Note that there is a second order dependence of the modulus on the diameters, thus small errors in these quantities can become large. The situation may be even more striking in the case of torque channel acquisition since the third order dependency appears in relations to determine the shear stress and modulus. Besides, the accuracy of measurement may be affected by clamping of specimens due to possible eccentricity of specimen, as discussed in ASTM E111-97 [76]. Clearly, the eccentricity induces a bending load to be superposed to axial load and disrupts the axial symmetry of the setup. Therefore, the measurement is influenced by relative rotational angles between the specimen, the extensometer, and the testing system (machine). Thus, it is advisable to determine elastic moduli using the same specimen and the same experimental setup as for yield surfaces determination and do not remove specimen from clamping.

In fact, it is common in experiments of yield surfaces detection that elastic moduli and zero offset strains are being determined directly during the experiment. The loading case to determine a particular yield surface point is usually referred to as the probe, and there are usually several probes per one specimen to determine the yield surface shape. Many authors even determine elastic moduli and zero offset strains for each probe separately, as can be seen in Wu and Yeh [23] and Gil et al. [48].

The typical procedure is as follows. At the beginning of the probe, four channels $\varepsilon^{\mathrm{tot}}$, γ^{tot}, σ, and τ are read and parameters E, G, ε_0, and γ_0 remain void. Therefore, offset strain in (6.9) is not being evaluated at the moment. As the load increases, experimental points are fitted by Hooke law using the least squares method. Note that modern testing systems are usually equipped with software modules that allow real-time evaluation of experimental data in some high-level programming language, e.g., C# and Python. Therefore, linear regression may be evaluated continuously, and the final values of elastic moduli and zero offset strains may be determined by different criteria from the regression. Sung et al. [25] used a stress threshold of about 5 MPa to restrict the range of experimental data for linear regression. Wu and Yeh [23] used the stress range of approximately 50% of the expected elastic domain. Also, it is possible to determine elastic moduli from regression as the maximum slope determined or by the minimum acceptable value of the *coefficient of determination*. Once the moduli and zero offset strains are determined, the values are substituted into Eq. (6.9) and continuous computation of the linear regression is terminated. Subsequently, as the probe goes on, a continuous computation of offset strain as in Eq. (6.9) is initiated. The probe is finished as soon as the yield criterion is met, i.e., when the offset strain reaches

ROOSTAEI, 978-0-12-819293-1

LaTeX class: roostaei, 2021/05/25 10:02:47 roostaei driver • file: roostaei06.tex (Renata) • Prn: 2021/07/12;14:50:04 • p. 16
pro: ROOSTAEI • model: a03 • color: 1c • ref-style: Numbered (Style 1) • lang: en-US • docsubty: CHP •

B978-0-12-819293-1.00016-4, 00006

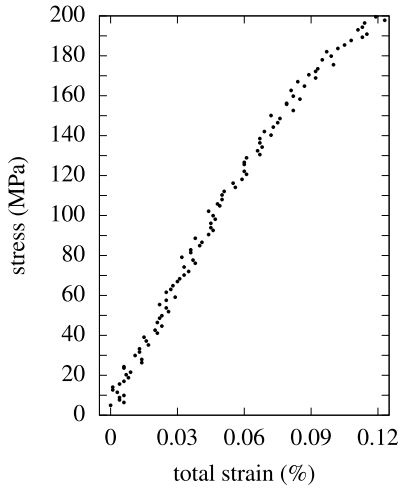

Figure 6.6 A detail of the stress–strain curve used to determine Young modulus map in Fig. 6.7.

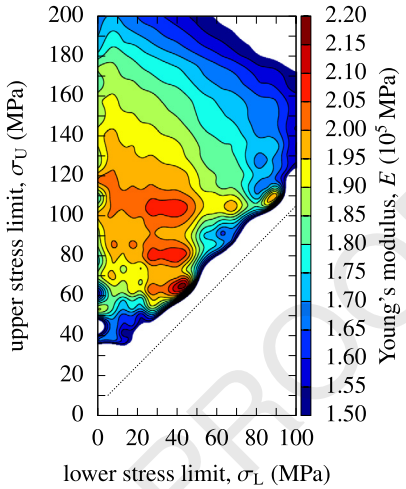

Figure 6.7 Map of Young modulus values dependence on lower and upper limits of the stress domain used for regression analysis.

the prescribed threshold. Note that using this approach, no interruption of loading is necessary. However, this approach requires the testing system to be able to perform real-time calculations with experimental data, evaluate conditional statements, and to have adequate feedback control.

It is clear that elastic moduli and zero offset strains are affected by the range of data used in linear regression. Thus, the lower stress limit should be set up in order to discard the data affected by backlash of the testing setup, initial grip alignment, and the loading onset. Likewise, the upper stress limit should be set up in order to restrict the regression to elastic domain. Wu and Yeh [23] analyzed the influence of the upper limit on the shear modulus G and reported variation within 3.4%. This analysis may be generalized as shown in Figs. 6.6 and 6.7.

Fig. 6.6 presents an example of stress–strain curve data gained from experimental setup. In Fig. 6.7, Young modulus values obtained by linear regression are given as a function of lower and upper limits of the stress domain used in regression analysis. It can be clearly seen that values of Young modulus vary with the upper and lower stress limits.

First, it is obvious in this example that regression analysis gives lower Young modulus values when the lower stress limit is zero, i.e., along the vertical line given by $\sigma_L = 0\,\text{MPa}$. This suggests that data acquisition at the beginning of reading was affected by hysteresis at loading onset. Further, the decrease of Young modulus values beyond the horizontal line at $\sigma_U = 110\,\text{MPa}$ is also obvious. This suggests that $\sigma_U = 110\,\text{MPa}$ determines the upper limit of the elastic domain. Besides, three peaks at (40, 65), (40, 80), and (40, 105) MPa may indicate some issue in data acquisition.

Note that there are many other factors affecting yielding evaluation which are not mentioned herein, e.g., mutual influence of subsequent probes due to plastic strain

LaTeX class: roostaei, 2021/05/25 10:02:47 roostaei driver • file: roostaei06.tex (Renata) • Prn: 2021/07/12;14:50:04 • p. 17
pro: ROOSTAEI • model: a03 • color: 1c • ref-style: Numbered (Style 1) • lang: en-US • docsubty: CHP •

B978-0-12-819293-1.00016-4, 00006

accumulation, mutual influence of elastic moduli under multiaxial loading, creep straining, loading rate, and probing paths pattern. For more information on procedures concerning elastic moduli determination and influence, the reader is referred to Wu and Yeh [23], Gil et al. [48], Sung et al. [25], and ASTM E111-97 [76].

6.2.5 Observed yield surface distortion

Experimental observations suggest that directional distortional hardening (DDH) is inherent to different metals, e.g., steels, pure aluminum, aluminum alloys, copper, brass, titanium, titanium alloys, and nickel alloys. Thus, it covers materials with various lattice systems, e.g., body-centered cubic (bcc), face-centered cubic (fcc), and hexagonal close-packed (hcp). Some degree of plastic anisotropy has been observed in polymers and soils as well. Although the anisotropy does not strictly match the definition of DDH, it has some key features in common, namely, complex or distorted shapes of yield surfaces.

Wu and Yeh [23] carried out experiments of yield surfaces detection on specimens made of type 304 stainless steel. First, they probed the yield surface of a virgin material and found that results are in good agreement with von Mises theory, i.e., the initial yield surface in σ–$\sqrt{3}\tau$ space is circular. Then, they subjected the same specimen to axial total strain of 0.2%, which induced the axial plastic strain of 540 $\mu\varepsilon$. After the prestrain, they used the same method to detect the yield surface as in the case of the virgin material. Unlike the test on the virgin material, the test on the prestrained steel revealed distortion of the circular shape of the yield surface. They conducted further testing on the same specimen with increasing prestrains. The higher prestrain applied, the higher distortion observed. In Fig. 6.8, the second subsequent yield surface is shown. Lissenden et al. [47] investigated specimens made of type 316 stainless steel. They used a biaxial stress loading trajectory to prestrain a virgin material. The distortion observed is shown in Fig. 6.9. Hu et al. [52] observed distortion in type 45 steel in normalized condition, as shown in Fig. 6.10. Some other results for various types of steels may be seen in Michno and Findley [34], Gupta and Lauert [77], Troshchenko and Kul'chitskii [38], and Wu et al. [24].

Also, DDH occurs in pure aluminum and its alloys. Phillips and Tang [21] studied an effect of loading path on the yield surface of pure aluminum at elevated temperatures. They concluded that increasing temperature shrinks the size of yield surfaces, while the distortion is not essentially affected by temperature rise. An example of the distorted yield surface determined at room temperature is given in Figs. 6.14 and 6.15. Khan et al. [51] investigated Al6061-T6511 aluminum alloy. They prestrained specimens by biaxial stress in σ–$\sqrt{3}\tau$ space, which caused distortion as shown in Fig. 6.11. More results from investigation on aluminum alloys may be seen in Phillips et al. [20], Phillips and Lu [22], Stout et al. [40], Brown et al. [50], and Wu [78].

Besides the investigations on steels and aluminum alloys, DDH was reported by Helling et al. [41] in experiments on 70:30 brass. Fig. 6.12 shows a yield surface from this test after shear prestraining. Dietrich and Kowalewski [46] detected distortion of yield surfaces in experiments on pure copper. An example of their results is given in

ROOSTAEI, 978-0-12-819293-1

LaTeX class: roostaei, 2021/05/25 10:02:47 roostaei driver • file: roostaei06.tex (Renata) • Prn: 2021/07/12;14:50:04 • p. 18
pro: ROOSTAEI • model: a03 • color: 1c • ref-style: Numbered (Style 1) • lang: en-US • docsubty: CHP •

B978-0-12-819293-1.00016-4, 00006

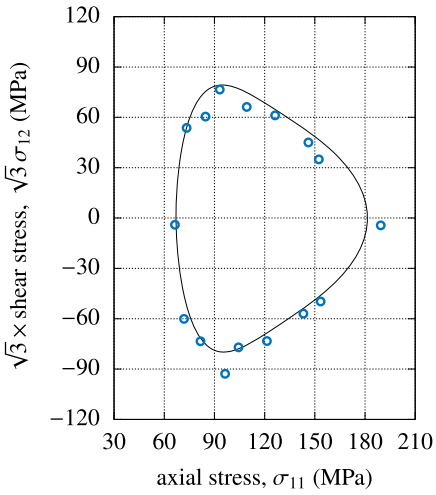

Figure 6.8 DDH in experiments on type 304 stainless steel by Wu and Yeh [23].

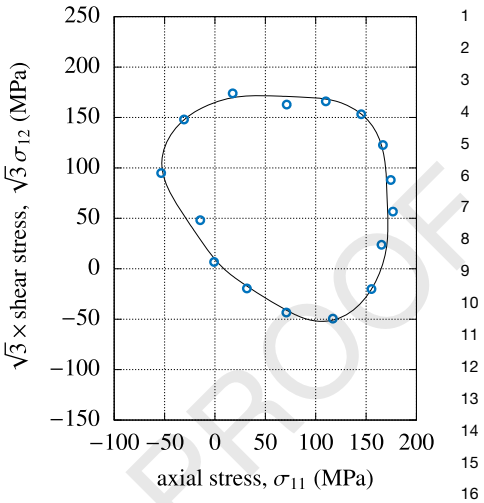

Figure 6.9 DDH in experiments on type 316 stainless steel by Lissenden et al. [47].

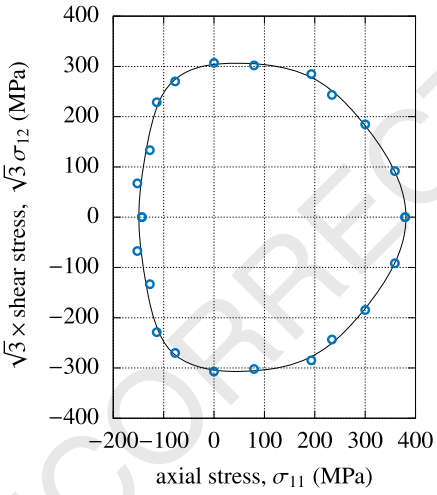

Figure 6.10 DDH in experiments on type 45 steel by Hu et al. [52].

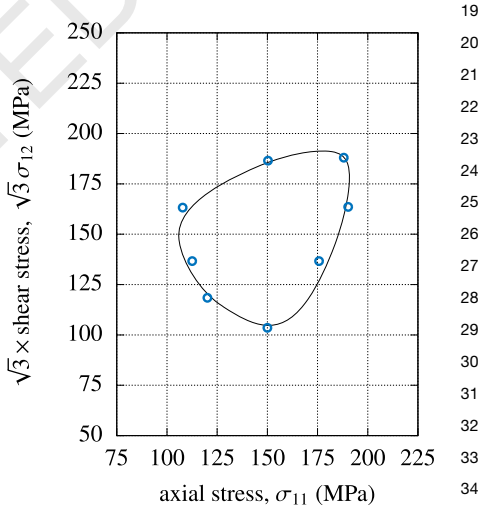

Figure 6.11 DDH in experiments on Al6061-T6511 alloy by Khan et al. [51].

Fig. 6.13. Some experiments on nickel-base superalloy Inconel 718 were reported by Gil et al. [48].

Some more experiments on other metals except steel and aluminum may be seen in Shiratori et al. [33], Phillips and Das [39], Khan and Wang [44], Khan et al. [79], Khan and Yu [80], and Khan et al. [81]. Also, distorted yield surfaces and yield surfaces with complex shapes—not necessarily evolved due to strain hardening—are reported in experiments carried out on polymers by Kolling et al. [82] and in experiments carried

LaTeX class: roostaei, 2021/05/25 10:02:47 roostaei driver • file: roostaei06.tex (Renata) • Prn: 2021/07/12;14:50:04 • p. 19
pro: ROOSTAEI • model: a03 • color: 1c • ref-style: Numbered (Style 1) • lang: en-US • docsubty: CHP •

B978-0-12-819293-1.00016-4, 00006

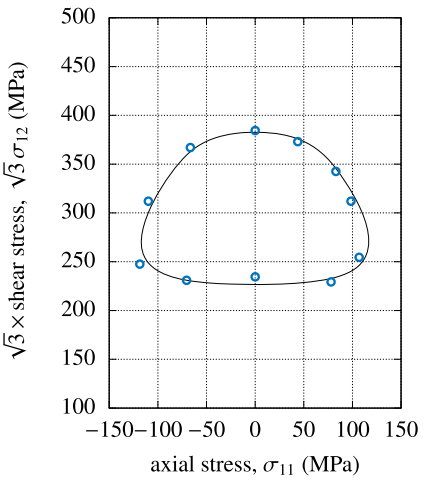

Figure 6.12 DDH in experiments on 70:30 brass by Helling et al. [41].

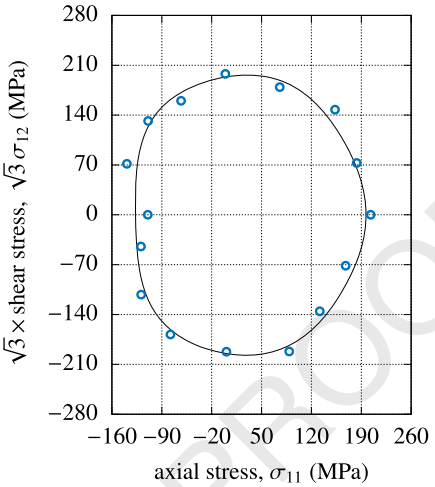

Figure 6.13 DDH in experiments on copper by Dietrich and Kowalewski [46].

out on soils by Pestana and Whittle [83], Taiebat and Dafalias [84], and Yao and Kong [85].

6.2.6 Synthesis of experimental results

The first experimental observations suggesting the distortion of yield surfaces due to plastic straining date back to the 1930s. Since then, many other experiments proved that yield surface distortion occurs in various metals and also polymers and soils. Many of the early experiments suggest the existence of corners in distorted yield surfaces, though there are discrepancies among experimental results in the decades since and most recent experiments not show corners in the yield surface, but do show the that the yield surface shape evolves asymmetrically (directional distortional hardening).

Although several experimental techniques were outlined in this chapter, most results were achieved by testing of thin-walled tubular specimens under combined axial load and torque. Further, factors that substantially affect accuracy of yield surfaces detection were outlined, including the definition of the onset of yield and the method used to determine the elastic moduli.

From the experimental results shown in Figs. 6.8–6.13 and Table 6.1 several conclusions can be drawn:

- Yield surface distortion is generally manifested by sharpening of yield surfaces in the direction of straining and flattening in the opposite direction (a.k.a. directional distortion, or DDH). In a few cases, e.g., Ishikawa [5] and Dietrich and Kowalewski [46], the yield surface distorts symmetrically, but most experiments on most materials show DDH.
- Yield surfaces can be highly pronounced even after small plastic strains. For example, Phillips and Tang [21] see DDH with only 0.0157% plastic strain.

ROOSTAEI, 978-0-12-819293-1

LaTeX class: roostaei, 2021/05/25 10:02:47 roostaei driver • file: roostaei06.tex (Renata) • Prn: 2021/07/12;14:50:04 • p. 20
pro: ROOSTAEI • model: a03 • color: 1c • ref-style: Numbered (Style 1) • lang: en-US • docsubty: CHP •

B978-0-12-819293-1.00016-4, 00006

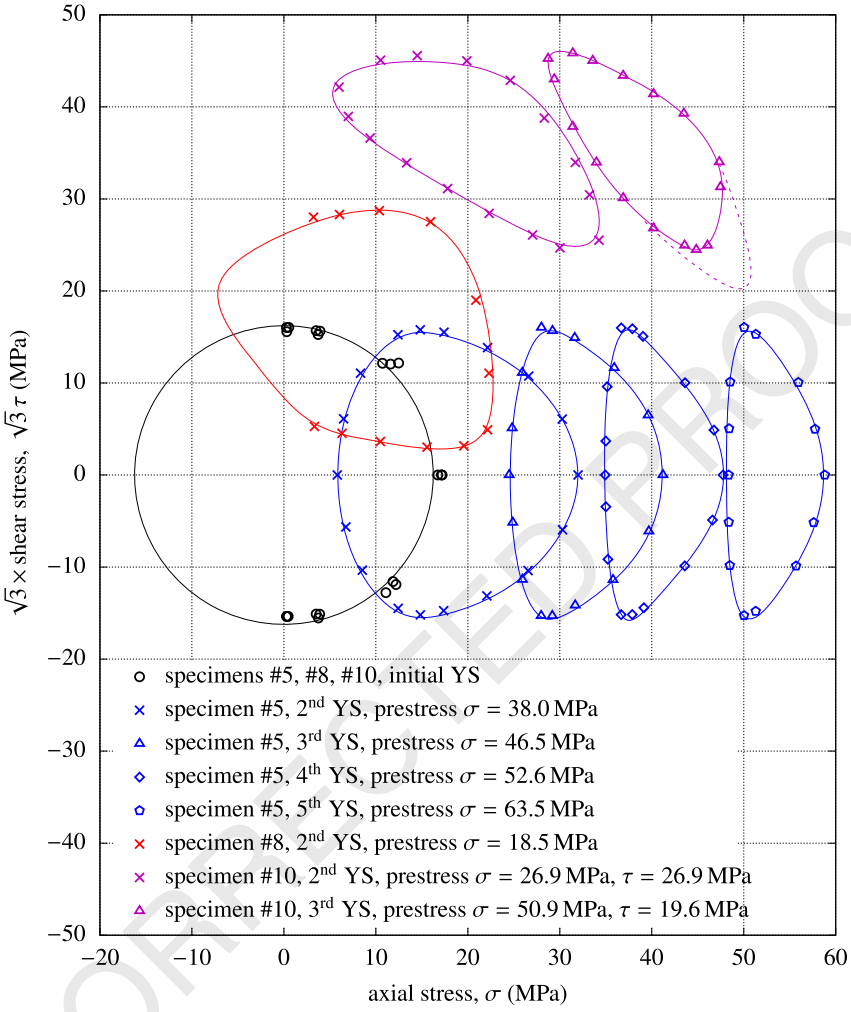

Figure 6.14 Directional distortional hardening (DDH) observed in experiments by Phillips and Tang [21] at ambient temperature of 21 °C. DDH is induced by two proportional prestraining trajectories and one nonproportional prestraining trajectory.

- Directional distortional hardening is coincident with the *Bauschinger effect*, i.e., both phenomena are being observed together.
- Distorted surfaces may completely drift off the origin of coordinate system due to extensive straining. Therefore, the onset of plastic strain may occur during unloading, before the material is reloaded in the opposite direction.
- Under proportional loading, directional distortional hardening preserves symmetry of the yield surface along the direction of loading. This axis of symmetry may be considered the main axis of the yield surface.

LaTeX class: roostaei, 2021/05/25 10:02:47 roostaei driver • file: roostaei06.tex (Renata) • Prn: 2021/07/12;14:50:04 • p. 21
pro: ROOSTAEI • model: a03 • color: 1c • ref-style: Numbered (Style 1) • lang: en-US • docsubty: CHP •

B978-0-12-819293-1.00016-4, 00006

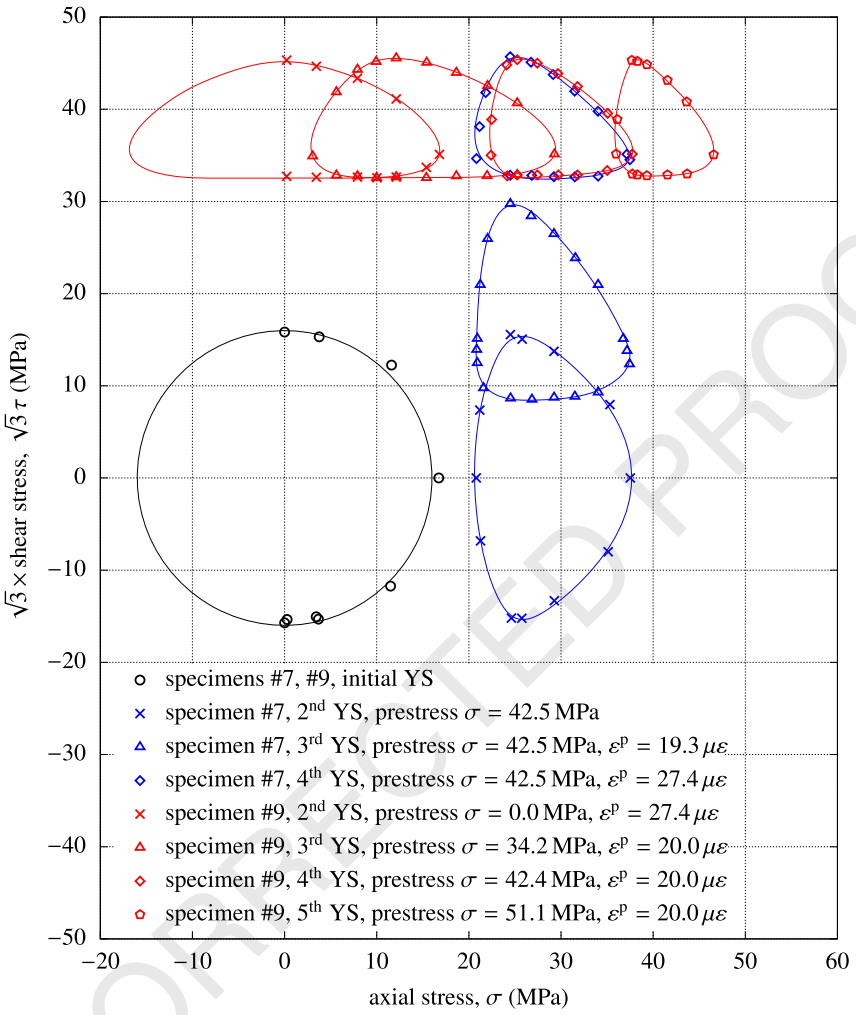

Figure 6.15 Directional distortional hardening observed in experiments by Phillips and Tang [21] at ambient temperature of 21 °C. DDH is induced by two nonproportional prestraining trajectories.

- Directional distortion seems to preserve convexity of yield surfaces, though, recently, some authors reported loss of convexity under large prestrains and fine definition of yielding.
- Yield surfaces often show shortening in the straining direction. This is called the cross-effect and can be seen regardless of whether or not DDH is observed.

These observations hold for many different materials, with different experimental techniques, and using different of definitions of yield. This suggests that DDH is a property common to metals and the modeling of this phenomenon may be important for accurately predicting plastic deformation in many materials.

ROOSTAEI, 978-0-12-819293-1

LaTeX class: roostaei, 2021/05/25 10:02:47 roostaei driver • file: roostaei06.tex (Renata) • Prn: 2021/07/12;14:50:04 • p. 22
pro: ROOSTAEI • model: a03 • color: 1c • ref-style: Numbered (Style 1) • lang: en-US • docsubty: CHP •

B978-0-12-819293-1.00016-4, 00006

6.3 Modeling of yield surface distortion

This section provides a concise review of some interesting concepts to mathematically generate yield surface distortion. These are divided into uniaxial and multiaxial types according to the number of directions associated with the distortion.

Also included is a new model dedicated to yield surface distortion that combines several attractive features of various theories from recent years. Both the theory and numerical implementation for this model are briefly presented. However, in order to meet the desired requirements (e.g., control of yield surface shape and accurately capturing a wide variety of experimentally found yield surfaces) the yield function is very complex, so for more details on this model and its numerical implementation the reader is encouraged to study an upcoming paper.

6.3.1 Notable models featuring uniaxial distortion

The distortion of the yield surface can somewhat differ in various materials and can be approached analytically in many different ways. The following text divides the models from the literature into those generated by distortional tensors that exhibit more implicit control over its shape, and those generated explicitly with concrete shape in mind which are therefore more controllable. For easier comparison, the forms of the explored yield functions may differ from those originally presented by the authors in order to ensure that they all use similar nomenclature and each share the definition of yield as $f = 0$.

6.3.1.1 High-order tensor approach to distortion generation

Early attempts to model the distortion of yield surfaces may be traced back to the work by Hill [10]. Motivated by observation of plastic anisotropy in components manufactured by forming process, he extended the von Mises yield criterion to the case of orthotropic plasticity. The proposed yield function is given by

$$2f = F(\sigma_y - \sigma_z)^2 + G(\sigma_z - \sigma_x)^2 + H(\sigma_x - \sigma_y)^2 + 2L\tau_{yz}^2 + 2M\tau_{zx}^2 + \\ + 2N\tau_{xy}^2 - 1, \tag{6.11}$$

where σ_α and $\tau_{\alpha\beta}$ are the stress tensor components, and F, G, H, L, M, and N are material parameters that control scaling in orthogonal directions. Note that the model inherits pressure insensitivity from the von Mises criterion.

A generalization enabling rotation of the scaled yield surface was proposed by Edelman and Drucker in [86] in the form

$$f = \tfrac{1}{2} A_{ijkl} \left(s_{ij} - m\varepsilon_{ij}\right) \left(s_{kl} - m\varepsilon_{kl}\right) - k^2, \tag{6.12}$$

where A_{ijkl} are components of the 4th order distortional tensor, s_{ij} is the deviatoric stress component, m is the Bauschinger parameter, and k is the isotropic hardening variable. Baltov and Sawczuk in [87] further developed the theory and used a deviatoric backstress tensor.

ROOSTAEI, 978-0-12-819293-1

LaTeX class: roostaei, 2021/05/25 10:02:47 roostaei driver • file: roostaei06.tex (Renata) • Prn: 2021/07/12;14:50:04 • p. 23
pro: ROOSTAEI • model: a03 • color: 1c • ref-style: Numbered (Style 1) • lang: en-US • docsubty: CHP •

B978-0-12-819293-1.00016-4, 00006

Evolution of this concept to feature sharpening of the front apex and flattening of the rear, was described by Williams and Svensson in [31,32]. The yield function is built according to statistical reasoning and takes the form

$$f = \left(I_{ijkl} + A_0 E^{\mathrm{p}}_{ij} E^{\mathrm{p}}_{kl}\right)\left(\sigma_{ij} + \alpha_{ij}\right)\left(\sigma_{kl} + \alpha_{kl}\right) - k^2, \tag{6.13}$$

where I_{ijkl} is the deviatoric identity tensor

$$I_{ijkl} = \delta_{ik}\delta_{jl} - \frac{1}{3}\delta_{ij}\delta_{kl}, \tag{6.14}$$

and A_0 is the anisotropic parameter, E^{p}_{ij} is the aggregate plastic strain tensor, and variable α_{ij} encompasses the kinematic and distortional effects as

$$\alpha_{ij} = E^{\mathrm{p}}_{ij}\left(L_{pqrs}\sigma_{pq}\sigma_{rs} - m\right), \tag{6.15}$$

with m the Bauschinger parameter and L_{pqrs} as the evolving distortional parameter, which is in effect scaling a projected part of the stress σ_{ij}. When anisotropic change driven by A_0 is applied, an oriented asymmetric (directional) distortion emerges. The yield function is generally nonconvex with a parasitic mirror image. This requires careful conditioning when evaluating the plastic part of trial stress.

A simpler approach [1] to induce the directional distortion was used by Feigenbaum and Dafalias as

$$f = (\mathbf{s} - \boldsymbol{\alpha}) : \left(\tfrac{3}{2}\mathbf{I} + (\mathbf{n}_{\mathrm{r}} : \boldsymbol{\alpha})\,\mathbf{A}\right)(\mathbf{s} - \boldsymbol{\alpha}) - k^2, \tag{6.16}$$

where $\mathbf{I}$ is the deviatoric tensor as in Eq. (6.14) (symmetrization can be applied), $\mathbf{A}$ is the 4th-order evolving anisotropic tensor, and $\mathbf{n}_{\mathrm{r}}$, given by

$$\mathbf{n}_{\mathrm{r}} = \frac{\boldsymbol{s} - \boldsymbol{\alpha}}{\|\boldsymbol{s} - \boldsymbol{\alpha}\|}, \tag{6.17}$$

is the deviatoric unit tensor along the radius $(\boldsymbol{s} - \boldsymbol{\alpha})$. The 4th order tensor $\mathbf{A}$ is responsible for distortion and a dot product of backstress and the unit radial stress tensor gives the direction to the distortion. In effect, the distortion is induced by various scaling by the anisotropic tensor according to the position of radial stress along the axis of the backstress. Adding a variable as $(c + \mathbf{n}_{\mathrm{r}} : \boldsymbol{\alpha})$ can utilize the anisotropic tensor to shorten the yield surface, which is desirable with more pronounced distortion. Still, the shape does not offer the more pronounced corners and flat rear seen in some of the experiments, e.g., Figs. 6.8, 6.9, and 6.11. Some other plasticity models with the yield criterion capable of capturing the distortion of yield surfaces may be seen in [88,89] and [6].

The early attempts to employ tensors of orders higher than four in constitutive modeling of mechanical behavior of materials may be traced back to Mālmeisters [90] and Gol'denblat and Kopnov [91]. Mālmeisters proposed the strength criterion in the form

$$f = \Pi_{ij}\sigma_{ij} + \Pi_{ijkl}\sigma_{ij}\sigma_{kl} + \Pi_{ijklmn}\sigma_{ij}\sigma_{kl}\sigma_{mn} + \cdots - 1, \tag{6.18}$$

ROOSTAEI, 978-0-12-819293-1

LaTeX class: roostaei, 2021/05/25 10:02:47 roostaei driver • file: roostaei06.tex (Renata) • Prn: 2021/07/12;14:50:04 • p. 24
pro: ROOSTAEI • model: a03 • color: 1c • ref-style: Numbered (Style 1) • lang: en-US • docsubty: CHP •

B978-0-12-819293-1.00016-4, 00006

where σ_{ij} are the stress tensor components, and $\Pi_{ij\ldots}$ are components of the even-order tensor-valued parameters that represent material properties.

Rees in [92] developed a plasticity model with the yield criterion given by

$$f = f_{\mathrm{s}}\left(F_1, F_2, F_3\right) - 1, \tag{6.19}$$

where

$$F_1 = \left(C_{ij} - A_{ij}\right)\left(s_{ij} - \alpha_{ij}\right), \tag{6.20}$$

$$F_2 = \frac{1}{2}\left(C_{ijkl} - A_{ijkl}\right)\left(s_{ij} - \alpha_{ij}\right)\left(s_{kl} - \alpha_{kl}\right), \tag{6.21}$$

$$F_3 = \frac{1}{3}\left(C_{ijklmn} - A_{ijklmn}\right)\left(s_{ij} - \alpha_{ij}\right)\left(s_{kl} - \alpha_{kl}\right)\left(s_{mn} - \alpha_{mn}\right), \tag{6.22}$$

where $C_{ij\ldots}$ are the components of isotropic tensors, $A_{ij\ldots}$ are the components of tensors responsible for the plastic anisotropy, s_{ij} are the deviatoric stress components, α_{ij} are the backstress components, and where three different expressions for f_{s} were used, namely, $f_{\mathrm{s}} = F_1 + F_2$, $f_{\mathrm{s}} = F_2 + F_3$, and $f_{\mathrm{s}} = F_1 + F_2 + F_3$.

Following the work in [90] and [91], Grewolls and Kreißig [93] and Shutov et al. [94] truncated the general polynomial expression after the cubic degree, which gives the yield function in the form

$$f = K_0\left(\varepsilon^{\mathrm{p}}_{\mathrm{eq}}\right) + K_{ij}\sigma_{ij} + K_{ijkl}\sigma_{ij}\sigma_{kl} + K_{ijklmn}\sigma_{ij}\sigma_{kl}\sigma_{mn}, \tag{6.23}$$

where $K_{ij\ldots}$ are components of material tensors of 2nd, 4th, and 6th order, and K_0 is a scalar-valued material parameter that depends on the equivalent plastic strain $\varepsilon^{\mathrm{p}}_{\mathrm{eq}}$. They used an approach by Danilov [95] to formulate evolution equations.

Note that in all the above models, only the yield function is presented. However, to complete the model and allow for yield surface distortion to evolve, hardening rules must also be supplied. The reader is encouraged to see the original papers for the description of the hardening rules. However, suffice to say that in most cases the hardening rule were simply assumed in order to capture the experimentally observed changes in the yield surface size, shape, and location. Some notable exceptions are the recent Lester and Scherzinger [96] or an earlier Feigenbaum and Dafalias model [1], where the evolution laws for models' internal variables were proposed so that the plastic straining would preserve the second law of thermodynamics equivalently expressed via the Clausius–Duhem inequality. This property is referred to as the thermodynamic consistency, and keeps the model consistent from the physical point of view. A number of assumptions about energy storage in the material go into the thermodynamic consistency, one of which states that the distortion of the yield surface causes less energy to be stored in the material or that distortion of the yield surface somehow releases rather than stores energy. This interesting assumption has not been verified experimentally.

6.3.1.2 Explicit control of yield distortion

The simplest way to generate distortion explicitly (with user control over the yield surface shape) is to use a function that defines radial stress according to its angular

ROOSTAEI, 978-0-12-819293-1

LaTeX class: roostaei, 2021/05/25 10:02:47 roostaei driver • file: roostaei06.tex (Renata) • Prn: 2021/07/12;14:50:04 • p. 25
pro: ROOSTAEI • model: a03 • color: 1c • ref-style: Numbered (Style 1) • lang: en-US • docsubty: CHP •

B978-0-12-819293-1.00016-4, 00006

position with respect to the distortion direction. Feigenbaum and Dafalias in [97] defined the yield function as

$$f = \tfrac{3}{2}\left[1 - c\left(\mathbf{n}_{\mathrm{r}} : \boldsymbol{\alpha}\right)\right](\boldsymbol{s} - \boldsymbol{\alpha}) : (\boldsymbol{s} - \boldsymbol{\alpha}) - k^2, \tag{6.24}$$

where c is a constant representing the amount of distortion in the yield surface. Note that this yield function did not arise as an explicit model, but Parma et al. [98] showed that it is solvable analytically and thus the model parameters can be chosen to get the desired shape of the yield surface.

Rather than modifying radial stress, one can get distortion by modifying the impact of the isotropic parameter k, as proposed by Ortiz and Popov in [99]. In this case, a scalar-valued multiplier $R^{\theta}(\boldsymbol{\rho}, \boldsymbol{\theta})$ expressed in terms of a Fourier series modifies the involvement of the isotropic parameter as

$$f = \|\mathbf{s} - \boldsymbol{\alpha}\| - k\left(1 + R^{\theta}(\boldsymbol{\rho}, \boldsymbol{\theta})\right) = \|\mathbf{s} - \boldsymbol{\alpha}\| - k\left(1 + \sum_{n=2}^{+\infty} \rho_n \cos n\theta_n\right), \tag{6.25}$$

where ρ_n are the coefficients of the Fourier series and θ_n are angles between the radial stress and the appropriate director as

$$\theta_n = \arccos\left(\mathbf{n}_{\mathrm{r}} : \mathbf{n}_{\mathrm{z}n}\right) \tag{6.26}$$

with $\mathbf{n}_{\mathrm{z}n}$ being the unit length representation of the director tensor $\mathbf{z}_n$. By default, these director tensors are considered identical and equal to backstress.

Let us now visualize the required coefficient $R^{\theta}(\boldsymbol{\rho}, \boldsymbol{\theta})$ to reach the radial stress yield limit for a perfect fit on experimental data. With a suitable fit of the isotropic parameter k and considering the position of backstress $\boldsymbol{\alpha}$ as half way between front apex and rear, the convex splines generated on the data in Fig. 6.14 are replotted accordingly in Fig. 6.16(a). Unfortunately, the structure of Eq. (6.25) does not work well with the presented experimental data shown in Fig. 6.16(a), in other words, Eq. (6.25) does not fit that data.

However, borrowing the idea from [99], a different function, $R(c, x)$, can be used to control the effect of the isotropic hardening term such as

$$f = \sqrt{\tfrac{3}{2}}\,\|\mathbf{s} - \boldsymbol{\alpha}\| - k\left(1 + R(c, x)\right), \tag{6.27}$$

with $x = \mathbf{n}_{\mathrm{r}} : \mathbf{n}_{\mathrm{z}}$, which equals the cosine of θ, and captures the directionality of the distortion. The shape of $R(c, x)$ needed to fit the experimental data in Fig. 6.14 is shown in Fig. 6.16(b), with k being calibrated from front and rear points of each yield surface (specimen #5) individually. A suitable isotropic softening rule has to be provided and calibrated. Multiplier $R(c, x)$ therefore reaches higher values for more pronounced distortion as the axial length of the YS shortens. While a function $R(c, x)$ that matches the shapes in Fig. 6.16(b) is within reach of basic phenomenological modeling, it has yet to be explored in detail and identified.

ROOSTAEI, 978-0-12-819293-1

LaTeX class: roostaei, 2021/05/25 10:02:47 roostaei driver • file: roostaei06.tex (Renata) • Prn: 2021/07/12;14:50:04 • p. 26
pro: ROOSTAEI • model: a03 • color: 1c • ref-style: Numbered (Style 1) • lang: en-US • docsubty: CHP •

B978-0-12-819293-1.00016-4, 00006

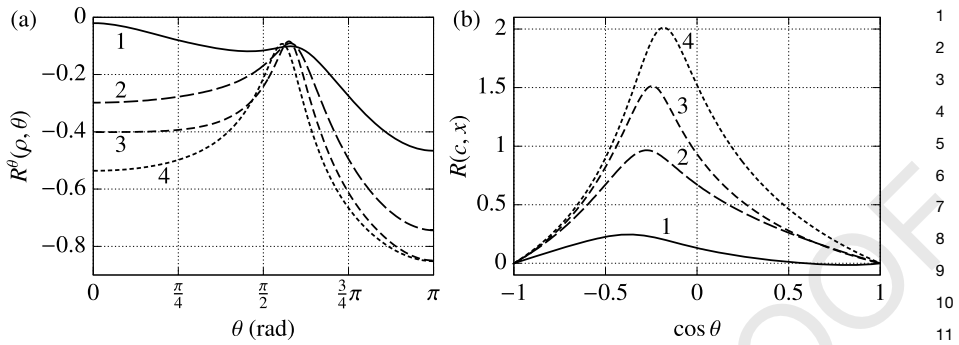

Figure 6.16 Two forms of distortion multiplier for radial stress yield limit for simple tension of pure aluminum after Phillips and Tang [21].

A model using orthogonal projection of the radial stress was proposed by François in [100]. The yield function is given by

$$f = \left\| \mathbf{s}^{\mathrm{d}} - \boldsymbol{\alpha} \right\| - k - \sigma_{\mathrm{y}}, \tag{6.28}$$

where $\mathbf{s}^{\mathrm{d}}$ is the distorted stress tensor, $\boldsymbol{\alpha}$ is the backstress, k is the isotropic hardening function, and σ_{y} is the initial yield stress. The distorted stress tensor is given by

$$\mathbf{s}^{\mathrm{d}} = \mathbf{s} + \boldsymbol{\alpha} \frac{\mathbf{s}^{\mathrm{y}} : \mathbf{s}^{\mathrm{y}}}{2X_1 \left(k + \sigma_{\mathrm{y}}\right)}, \tag{6.29}$$

where $\mathbf{s}^{\mathrm{y}}$ is an orthogonal part of the deviatoric stress tensor $\mathbf{s}$ given by

$$\mathbf{s}^{\mathrm{y}} = \mathbf{s} - \mathbf{s}^{\mathrm{x}}, \tag{6.30}$$

where $\mathbf{s}^{\mathrm{x}}$ is the collinear part of the deviatoric stress tensor $\mathbf{s}$ with respect to the backstress tensor $\boldsymbol{\alpha}$ given by

$$\mathbf{s}^{\mathrm{x}} = \boldsymbol{\alpha} \frac{\mathbf{s} : \boldsymbol{\alpha}}{\boldsymbol{\alpha} : \boldsymbol{\alpha}}. \tag{6.31}$$

The stress tensor is therefore rescaled in the direction of distortion in an intensity controlled by internal variable X_1, proportionally to a square of the distance from the main axis. With a more complex function and with X_1 being a function of the collinear projection of radial stress, all imaginable shapes could be acquired. The fact that the distortion does not change points lying on the main axis means this model can skip calculation of distortion for proportional cyclic loading, which is convenient from the computational as well as calibrational point of view. Unfortunately, the yield function is not convex. Evaluating the plastic part of trial stress would require complex conditioning when large increments of trial stress are proposed.

Using a geometric approach, a new yield surface created as a weighted average between nominal von Mises and a pronounced form defined by arc sections is proposed

LaTeX class: roostaei, 2021/05/25 10:02:47 roostaei driver • file: roostaei06.tex (Renata) • Prn: 2021/07/12;14:50:04 • p. 27
pro: ROOSTAEI • model: a03 • color: 1c • ref-style: Numbered (Style 1) • lang: en-US • docsubty: CHP •

B978-0-12-819293-1.00016-4, 00006

by Shutov and Ihlemann in [101]. The model captures viscoplastic behavior and nearly any shape of distortion. Moreover, this model is provided with a strict proof of thermodynamic consistency.

It can be argued, that during proportional loading reversal, the material retains some of the induced anisotropy oriented in the loading direction and before the directional distortion evolves in the opposite direction, a simple distortion emerges, rather than a fully restored von Mises sphere. A variable axial scaling of the yield surface imitating such behavior is featured in Yeh et al. [102].

6.3.2 Modeling multiaxial distortion

Kurtyka and Życzkowski published a model [103] capable of capturing proportional expansion, translation, affine deformation, rotation, and distortion of the yield surface. The model employs stress vectors expressed in terms of Ilyushin five-dimensional stress space, with vector indices $i, j, k, l = 1, \ldots, 5$, where summation over repeated indices is implied. The yield criterion employed in this model is given by

$$f = (\sigma_i - a_i)\, Q_{ji}\, D_{jk}\, Q_{kl}\, (\sigma_l - a_l) - 1, \tag{6.32}$$

where σ_i are elements of the deviatoric stress vector, a_i are elements of the backstress vector, Q_{ij} are elements of the rotation matrix, and D_{jk} are elements of the diagonal functional matrix. The authors used purely geometric description of transformations of the yield surface, and, later on, they proposed evolution equations for the model internal variables. The model offers 5 orthogonal directions of distortion. So unlike previous models discussed, this model can have regions of sharpening/flattening in multiple directions, and thus we consider it a multiaxial distortion model. A very positive attribute of this model is its natural convexity.

We also examined a multidirectional sequential distortion using an approach that resembled that of Yeh et al. [102] but with smoother shapes. Although the yield function we derived was able to fit the data in Figs. 6.14 and 6.15 very well, the idea of assigning a small number of ordered distortion directors to a general loading trajectory smoothly and consistently is still an open problem.

Finally, while it is not multiaxial distortion of the yield surface, Section 6.3.6 discusses some possible means to get a similar effect on strain through other means.

6.3.3 Yield surface convexity

Convexity of the yield surface is not a law of nature, but rather comes from assumptions about normality, stability, and irreversibility. The convexity requirement originally arose from Prager surpassed condition of irreversibility [104], stating that plastic work done should always be positive. However, the convexity requirement is usually attributed to Drucker stability postulate in conjunction with the normality rule, stated in [105]. Due to the yield being just a concept, a general trajectory within the agreed elastic region may still accumulate small residual plastic strain. Depending on the measurement method used, this residual plastic strain will exceed the expected

ROOSTAEI, 978-0-12-819293-1

LaTeX class: roostaei, 2021/05/25 10:02:47 roostaei driver • file: roostaei06.tex (Renata) • Prn: 2021/07/12;14:50:04 • p. 28
pro: ROOSTAEI • model: a03 • color: 1c • ref-style: Numbered (Style 1) • lang: en-US • docsubty: CHP •

B978-0-12-819293-1.00016-4, 00006

level at a yield point and therefore suggest a sudden concavity in the yield surface. Alternatively, a normality rule may not hold.

However, for the stability of numerical algorithms employed in stress corrections, as well as when dividing trial stress into elastic and plastic part, the convexity of the yield function is crucial, see Plešek and Křístek [106]. The sufficient and necessary condition for convexity is that the Hessian matrix is positive definite in all relevant regions. Rather than conditioning eigenvalues, it is much more feasible to fulfill this condition by

$$\forall \boldsymbol{\phi} \neq \mathbf{0}: \ \boldsymbol{\phi} : \mathbf{H}\boldsymbol{\phi} > 0, \tag{6.33}$$

where $\boldsymbol{\phi}$ is an arbitrary second-order tensor. The structure of this condition enables normalizing $|\boldsymbol{\phi}| = 1$, which simplifies the analysis. If the distorted yield function is expected to have a convexity violation on its main axis, then the inequality in (6.33) can be expected to be further simplifiable.

This topic was explored in Plešek et al. [107], where it was applied on DDH yield functions of models from Feigenbaum–Dafalias family. Although the convexity of yield functions is not inherent to these models, some necessary and sufficient conditions imposed on models' parameters were found, so that the yield function convexity would be preserved. In their work, eventual rotational symmetry is capitalized by simplification of numerical search.

6.3.4 Showcase model of uniaxial distortion

In order to evaluate the effect of directional distortional hardening on multiaxial ratcheting predictions one should directly compare model predictions to those made using a nondistorted model. For a direct comparison, both models should share the same calibration of the kinematic hardening rule for backstress. To accomplish this, the distance from the front apex to the center denoted by backstress and the distance from the rear of the yield surface to the center need to stay unchanged. Moreover, even the gradient norms in the front and back points need to stay constant to keep the equality of these two models in proportional loading. Many yield function proposals, such as Feigenbaum and Dafalias [97], can actually utilize the higher value of gradient in the flattened rear to increase the rate of kinematic hardening during reversal. This depends on the applied evolution rules and their use of the gradient norm.

The gradient norm can also be eliminated from the flow-rule using the unit normal formulation,

$$\dot{\boldsymbol{\varepsilon}} = \lambda \mathbf{n}, \tag{6.34}$$

where $\mathbf{n}$ is the unit outer normal to the yield surface. Unlike the well-known relations employed in the integration of the aforementioned model in Marek et al. [108], the new model will define its stress response as

$$\dot{\boldsymbol{\sigma}} = \mathbf{C}\dot{\boldsymbol{\varepsilon}} - \lambda \mathbf{C}\mathbf{n}, \tag{6.35}$$

ROOSTAEI, 978-0-12-819293-1

LaTeX class: roostaei, 2021/05/25 10:02:47 roostaei driver • file: roostaei06.tex (Renata) • Prn: 2021/07/12;14:50:05 • p. 29
pro: ROOSTAEI • model: a03 • color: 1c • ref-style: Numbered (Style 1) • lang: en-US • docsubty: CHP •

B978-0-12-819293-1.00016-4, 00006

with the plastic multiplier

$$\lambda = \frac{\frac{\partial f}{\partial \boldsymbol{\sigma}} : \mathbf{C}\dot{\boldsymbol{\varepsilon}}}{K_p + \frac{\partial f}{\partial \boldsymbol{\sigma}} : \mathbf{C}\mathbf{n}}. \tag{6.36}$$

Starting with these requirements, a new concept for the yield function came to mind, borrowing an idea from Shutov and Ihlemann [101]. In their case, the distorted yield function was a weighted average between nominal von Mises and a fully distorted shape created by arc sections. The new approach keeps the yield function defined by arc sections during the whole evolution of distortion. For some cases, this offers very simple gradients, analytical solutions for radial return correction as well as the evaluation of plastic part of trial stress. The front apex is shaped by a hyperbolic arc. To avoid quartic equations when joining conics together, the evolution of distortion is driven by variables that need to keep some narrowly defined relations between each other. This is managed during calibration process rather than by the yield function itself.

As the yield function is segmented, it requires different rules depending on which region is active. Some of these rules are computationally expensive. Fortunately, they are mostly in scalar form with room for optimization. This subsection gives only a brief overview of this model, as details will be presented in an upcoming article.

6.3.4.1 *Yield function proposal*

The yield function is C^1 continuous and it is defined in unitless space of two scalar variables x, y. The yield function returns a value by decomposing the radial stress $\mathbf{s} - \boldsymbol{\alpha}$ into normalized axial and orthogonal projections with respect to the direction of distortion as

$$x = \sqrt{\tfrac{3}{2}}\,(\mathbf{s} - \boldsymbol{\alpha}) : \mathbf{n}_z / k \tag{6.37}$$

and

$$y = \sqrt{\tfrac{3}{2}}\,(\mathbf{s} - \boldsymbol{\alpha}) : \mathbf{n}_c / k, \tag{6.38}$$

with

$$\mathbf{n}_c = \frac{\sqrt{\frac{3}{2}}\,(\mathbf{s} - \boldsymbol{\alpha})\,/k - x\mathbf{n}_z}{\left\| \sqrt{\frac{3}{2}}\,(\mathbf{s} - \boldsymbol{\alpha})\,/k - x\mathbf{n}_z \right\|}, \tag{6.39}$$

where $\mathbf{s}$ is the deviatoric stress, $\boldsymbol{\alpha}$ is the deviatoric backstress, k is the isotropic variable initially defining yield stress, $\mathbf{n}_z$ is a unit tensor representing the direction $\mathbf{z}$, which determines the orientation and intensity of the distortion and is defined in Algorithm 6.1, and $\mathbf{n}_c$ is the orthogonal unit tensor in crosswise direction. The yield function is given in Algorithm 6.2 with internal variables defined in Algorithm 6.1. Fig. 6.17 shows the

ROOSTAEI, 978-0-12-819293-1

LaTeX class: roostaei, 2021/05/25 10:02:47 roostaei driver • file: roostaei06.tex (Renata) • Prn: 2021/07/12;14:50:05 • p. 30
pro: ROOSTAEI • model: a03 • color: 1c • ref-style: Numbered (Style 1) • lang: en-US • docsubty: CHP •

B978-0-12-819293-1.00016-4, 00006

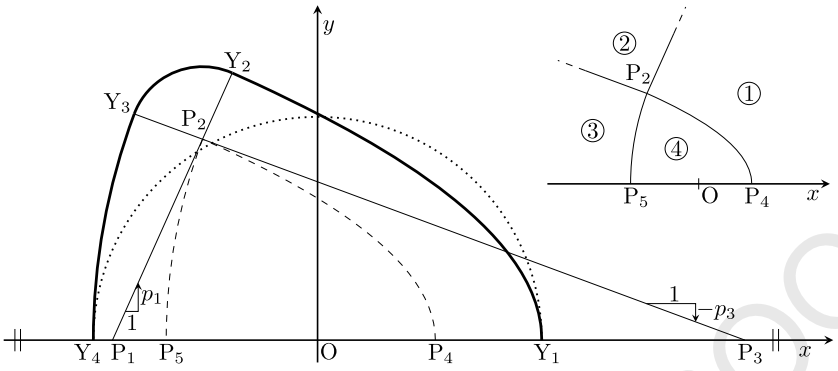

Figure 6.17 Structure of the segmented yield function.

yield surface profile ($f = 0$) in the x, y space comprising the curves connecting the points $\mathrm{Y}_1, \mathrm{Y}_2, \mathrm{Y}_3, \mathrm{Y}_4$, which includes two circular arcs $\mathrm{Y}_2\mathrm{Y}_3$ and $\mathrm{Y}_3\mathrm{Y}_4$ with centers P_2 and P_3, respectively, and a hyperbolic arc $\mathrm{Y}_1\mathrm{Y}_2$ which is a central projection from point P_1 of the control hyperbole $\mathrm{P}_4\mathrm{P}_2$ defined by

$$x = -a\sqrt{b^2 + y^2} + ab + 1, \tag{6.40}$$

where a, b belong to the internal dependent variables updated via Algorithm 6.1.

The evolving shape of the yield function is controlled by six parameters: c_0 controls the intensity of distortion in regards to the norm of the director tensor $\mathbf{z}$, c_1 and c_2 control the width and the flattening of the rear of the yield surface by positioning point $\mathrm{P}_2\left[\mathrm{x}_2, \mathrm{y}_2\right]$. Parameter c_3 controls the radius $r_2 = |\mathrm{Y}_2\mathrm{P}_2|$. Parameters c_4 and c_5 act to keep a narrow region of possible solutions of the hyperbolic apex by controlling the slope p_1. If p_1 is too low, the hyperbolic apex excessively sharpens. If p_1 is too large, the apex is more blunt, forcing it to become elliptic. To fulfill a convexity condition, only a few necessary conditions limiting the movement and radii of the two circular arcs and a condition for the solvability of the hyperbolic arc are needed.

In region 1, a radial return projection is used to obtain the value of the yield function. A projected stress point $[x_{\mathrm{RR}}, p\,(x_{\mathrm{RR}} - x_1)]$ is reached by central projection defined by point P_1. It is further used in Euler forward rule when applying stress correction after an integration step induced evolution of internal variables. Using stress projection instead of gradient return or closest point projection was deemed acceptable, as the difference is negligible, even more so with sufficiently small integration step. An ideal direction of stress correction varies according to actual situation. For regions 2 and 3, simple central projection is applied. Stress correction from region 4 is not implemented, as it may lack definition of direction and may induce bifurcation should the initial stress point reach point P_2. If it is required during simulation, it suggests problems with integration step length or with calibration, as r_2 becomes very small and region 4 fills most of the elastic region. In such a case, however, potential loading from region 2 would mean extreme sensitivity on the position of initial point

ROOSTAEI, 978-0-12-819293-1

LaTeX class: roostaei, 2021/05/25 10:02:47 roostaei driver • file: roostaei06.tex (Renata) • Prn: 2021/07/12;14:50:05 • p. 31
pro: ROOSTAEI • model: a03 • color: 1c • ref-style: Numbered (Style 1) • lang: en-US • docsubty: CHP •

B978-0-12-819293-1.00016-4, 00006

1. $\mathbf{z} = \boldsymbol{\alpha}_2 + \boldsymbol{\alpha}_3$
2. $c = c_0 \|\mathbf{z}\|$
3. **if** $c < 10^{-8}$
  a. $h = \sqrt{x^2 + y^2}$, $f = h - r_2$
  b. $x_{\mathrm{RR}} = hx$, $y_{\mathrm{RR}} = hy$
  c. **return**
4. $\mathbf{n}_z = \mathbf{z}/\|\mathbf{z}\|$, $x_2 = -c_1 c_2 c$, $y_2 = c_1 c$, $r_2 = 1 - c_3 c$, $p_1 = (c_4 + c_5 c)\ \sqrt[4]{c}$
5. $x_1 = x_2 - \dfrac{y_2}{p_1}$, $x_3 = \dfrac{x_2^2 + y_2^2 - (r_2 - 1)^2}{2(1 + x_2 - r_2)}$, $x_4 = x_2 + \dfrac{r_2}{\sqrt{p_1^2 + 1}}$,
$y_4 = y_2 + \dfrac{p_1 r_2}{\sqrt{p_1^2 + 1}}$
6. $a = \sqrt{\dfrac{2y_4}{p_1(1 - x_4)} - \left(\dfrac{y_4}{1 - x_4}\right)^2}^{-1}$, $h = \dfrac{x_4 - x_1}{x_2 - x_1}$, $p_3 = \dfrac{y_2}{x_2 - x_3}$, $r_3 = 1 + x_3$
7. $b = y_4 \sqrt{\dfrac{a^2}{p_1^2} - 1}$

Algorithm 6.1. INITIALIZE MODEL.

of loading. That is not expected to be a real property of a polycrystal material and therefore any calibration forcing r_2 to become too small is deemed incorrect. When new trial stress is analyzed, its plastic part may be evaluated either numerically or for some special cases, analytically. If the direction $\boldsymbol{\sigma}^{\mathrm{trial}} - \boldsymbol{\sigma}_0$ is parallel to the actual $\mathbf{n}_z, \mathbf{n}_c$ plane, it is easy to calculate solutions for pairs of $\boldsymbol{\sigma}_0$ and $\boldsymbol{\sigma}^{\mathrm{trial}}$ for which $\mathrm{f}(\boldsymbol{\sigma}_0) < 0$ and $\mathrm{f}(\boldsymbol{\sigma}^{\mathrm{trial}}) > 0$, defined by their respective relevant region IDs: $(1 \to 1)$, $(4 \to 1)$, $(2 \to 2)$, $(3 \to 3)$, and $(4 \to 3)$. Further combinations are possible to derive with more complex conditioning. In all cases, standard numerical procedure for finding the initial yield point is valid, as the yield function is convex and smooth. The model can be outfited with a long list of kinematic hardening rules. The particular choice for this chapter is explained in Section 6.3.6.1.

6.3.5 Evolution rules for distortion

There is very little known about the speed in which directional distortion evolves or changes direction. One comparison is kinematic hardening. In pure aluminum, a very pronounced distortion at the second prestress level in Fig. 6.14 formed in just over 200 με. Like kinematic hardening, distortional hardening is expected to continue evolving at ever receding rate. When kinematic hardening is simulated by great many components of Armstrong–Frederick type evanescent memory, each such component represents a subgroup of slip systems. Similar conditions may also carry a piece of information about the partial directional distortion. A smart rule that would limit ro-

ROOSTAEI, 978-0-12-819293-1

LaTeX class: roostaei, 2021/05/25 10:02:47 roostaei driver • file: roostaei06.tex (Renata) • Prn: 2021/07/12;14:50:05 • p. 32
pro: ROOSTAEI • model: a03 • color: 1c • ref-style: Numbered (Style 1) • lang: en-US • docsubty: CHP •

B978-0-12-819293-1.00016-4, 00006

1. Evaluate

a. $x = \sqrt{\frac{3}{2}}\,(\mathbf{s}-\boldsymbol{\alpha}):\mathbf{n}_z/k$

b. $y = \left\| \sqrt{\frac{3}{2}}\,(\mathbf{s}-\boldsymbol{\alpha})/k - x\mathbf{n}_z \right\|$

c. IF $y > 10^{-8}$ THEN $\quad \mathbf{n}_c = \left(\sqrt{\frac{3}{2}}\,(\mathbf{s}-\boldsymbol{\alpha})/k - x\mathbf{n}_z \right)/y$

2. Find active region:

IF $y \geq p_1\,(x-x_1) \ \wedge \ y \geq p_3\,(x-x_3)$

a. Region 2: $k_{\mathrm{RID}} \leftarrow 2$, $f = \left(\sqrt{(x-x_2)^2 + (y-y_2)^2} - r_2 \right) k$

ELSEIF $y < p_3\,(x-x_3) \ \wedge \ (x-x_3)^2 + y^2 > (r_3 - r_2)^2$

b. Region 3: $k_{\mathrm{RID}} \leftarrow 3$, $f = \left(\sqrt{(x-x_3)^2 + y^2} - r_3 \right) k$

ELSEIF $x > \left(-a\sqrt{b^2 + h^2 y^2} + ab + 1 + (g-1)\,x_1 \right)/h$

c. Region 1: $k_{\mathrm{RID}} \leftarrow 1$, $p = \dfrac{y}{x - x_1}$

d. $A_{\mathrm{RR}} = 1 - a^2 p^2$, $B_{\mathrm{RR}} = a^2 p^2 x_1 - ab - 1$, $C_{\mathrm{RR}} = 2ab + 1 - a^2 p^2 x_1^2$

e. $D_{\mathrm{RR}} = \sqrt{B_{\mathrm{RR}}^2 - A_{\mathrm{RR}} C_{\mathrm{RR}}}$

f. $x_{\mathrm{RR}} = \dfrac{-B_{\mathrm{RR}} - D_{\mathrm{RR}}}{A_{\mathrm{RR}}}$

g. $f = \dfrac{khr_2\,(x - x_{\mathrm{RR}})}{(x_{\mathrm{RR}} - x_1)\,(h-1)}$

ELSE

h. Region 4: $k_{\mathrm{RID}} \leftarrow 4$, $f = -r_2 k$

Algorithm 6.2. YIELD CONDITION.

tation of these components may lead to some temporal preservation of several distinct directions of distortion seen in Fig. 6.15.

6.3.5.1 *Effect of distortion on proportional stress response*

During proportional unloading and reloading in the opposite direction, at some point, the distortion director goes through zero and changes orientation. If the distortion of the yield function affects the position of the front apex or rear, this may cause a discontinuity in the stress response. In other words, the speed in which the rear of the yield surface loses its flattened shape and returns to normal von Mises has to be equal to the speed in which the front apex is beginning to rise in order for this transition to be smooth. For a general yield function based on von Mises theory,

$$f = \sqrt{\tfrac{3}{2}} A\,(c, \mathbf{z}, \mathbf{r})\,\|\mathbf{r}\| - k, \tag{6.41}$$

ROOSTAEI, 978-0-12-819293-1

B978-0-12-819293-1.00016-4, 00006

where A is a general distortion function, c is the distortion signal, $\mathbf{z}$ is the distortion director and $\mathbf{r}$ the radial stress tensor (i.e., $\mathbf{s}-\boldsymbol{\alpha}$), the following condition is therefore required:

$$\left.\frac{\partial \mathrm{f}}{\partial c}\right|_{c=0,\mathbf{r}=\sqrt{\frac{2}{3}}k\mathbf{n}_z} = -\left.\frac{\partial \mathrm{f}}{\partial c}\right|_{c=0,\mathbf{r}=-\sqrt{\frac{2}{3}}k\mathbf{n}_z}. \tag{6.42}$$

This condition could be circumvented by slowing down the speed of evolution of the distortion signal c whenever it is close to zero. However, this does not hold well as it may induce humps in the stress response.

6.3.5.2 Controlling uniaxial distortion

Although the evolution of yield surface shape is much more complex than what is captured by a uniaxial distortion, it is expected to be mostly symmetric after sufficient plastic straining in constant direction. Data clearly show the distortion director may even become nonparallel to the backstress. A meaningful examination and proposition of a rule controlling the direction and intensity of distortion most likely requires extensive experimental examination of subsequent intermediate yield surface shapes.

In Shutov and Ihlemann [101], the distortion is controlled by director tensor, for which the evolution rule is created by two-dimensional rheological analogy. This is a handy approach that could be used in various applications in material modeling.

In the new presented model, a simple relation of $\mathbf{z}=\boldsymbol{\alpha}_2+\boldsymbol{\alpha}_3$ is used to define the direction of the distortion. With an assumed ordering of the backstress components according to their evolution speeds, the director $\mathbf{z}$ leaves out the fastest first component as well as the forth, which exhibits slow constant movement before reaching threshold, reminiscent of a bounding surface. The slow movement can provide the observed decoupling of the direction of distortion from the origin of stress space. No dedicated terms were introduced, as an extensive experimental evidence would be needed to propose a rule with a logical structure.

6.3.6 Modeling the effect of distortion by other methods

As it turns out, the distortion can become a byproduct of a regular kinematic hardening (KH) rule without the need for terms importing further anisotropy or exotic modifications of the associative flow rule. In this case the yield surface is still the von Mises shape (circular in σ–$\sqrt{3}\tau$ space), but the effect of distortion on the plastic strain can be captured by changing the KH rule asymmetrically.

A multisurface kinematic hardening rule presented by Zhang et al. in [109] induces a similar effect to yield surface distortion that emerges from the use of great many components. They were able to retrace an experiment of Wu and Yeh [23] including probing paths with very fine yield point definition of just $3.5\,\mu\varepsilon$ effective plastic strain. Freund et al. in [110] mimicked distortion induced by a uniaxial plasticity model by employing it simultaneously over a set of 50 representative directions. Such an approach has large memory requirements but showed good conformity in the stress space in a tension–torsion (butterfly) ratcheting experiment.

ROOSTAEI, 978-0-12-819293-1

LaTeX class: roostaei, 2021/05/25 10:02:47 roostaei driver • file: roostaei06.tex (Renata) • Prn: 2021/07/12;14:50:05 • p. 34
pro: ROOSTAEI • model: a03 • color: 1c • ref-style: Numbered (Style 1) • lang: en-US • docsubty: CHP •

B978-0-12-819293-1.00016-4, 00006

Remarkable capabilities of a plane stress model based on crystal plasticity were demonstrated by Dluzewski in [111] by a controlled movement of up to 30 individual slip systems. The observed yield surface deformation exhibited very similar behavioral traits to the experimental data in Fig. 6.15. A more recent work in Liu et al. [112] can also exhibit two distinct directions of distortion.

6.3.6.1 A simple proposal for mimicking distortion

For all demonstrations in this chapter, the newly introduced model uses the multicomponent Armstrong–Frederick KH rule designated "MAFTr" by Dafalias and Feigenbaum [113]. In that paper it was shown that the MAFTr KH rule fit cyclic plastic data better than many other multicomponent Armstrong–Frederick-type kinematic hardening rules. Strictly for the purpose of this very section, a modification was added to gain the option to mimic the effect that distortion has on the strain without the need for employing the distortion of the yield surface.

The most straightforward approach to mimic the effect that distortion has on the plastic strain is to adjust the backstress evolution rate according to the angular orientation of the stress point with respect to the main axis of the intended distortion. In order to reach that, we modify the MAFTr KH rule by adding a multiplier $h_\alpha(c)$ as a function of the distortion signal c defined in Section 6.3.4. The MAFTr kinematic hardening rule now takes the following form:

$$\dot{\boldsymbol{\alpha}}_i = \langle\lambda\rangle\sqrt{\tfrac{2}{3}}h_\alpha c_i^\alpha \left\{\sqrt{\tfrac{2}{3}}a_i^S\mathbf{n} - [r_i\boldsymbol{\alpha}_i + (1-r_i)\,(\boldsymbol{\alpha}_i{:}\mathbf{n})\,\mathbf{n}]\right\}\ (i=1,2,3)\,, \quad (6.43)$$

$$\dot{\boldsymbol{\alpha}}_4 = \langle\lambda\rangle\sqrt{\tfrac{2}{3}}h_\alpha c_4^\alpha \left\{\sqrt{\tfrac{2}{3}}a_4^S\mathbf{n} - [r_4\boldsymbol{\alpha}_4 + (1-r_4)\,(\boldsymbol{\alpha}_4{:}\mathbf{n})\,\mathbf{n}]\left\langle 1 - \sqrt{\tfrac{2}{3}}\frac{\bar{a}}{\|\boldsymbol{\alpha}_4\|}\right\rangle\right\}, \quad (6.44)$$

with $r_i = \|\boldsymbol{\alpha}_i\|/a_i^{\mathrm{S}}$, where c_i^α control the rates of evolution and a_i^{S} control the asymptotic limits of backstress components so that

$$\left\|\boldsymbol{\alpha}_i^{\lim}\right\| = \sqrt{\tfrac{2}{3}}a_i^{\mathrm{S}} \quad (i=1,2,3)\,. \quad (6.45)$$

The fourth component exhibits initially linear hardening before reaching its threshold $\left\|\boldsymbol{\alpha}_4^{\mathrm{th}}\right\| = \sqrt{\frac{2}{3}}\bar{a}$ and continues to its asymptotic limit at

$$\left\|\boldsymbol{\alpha}_4^{\lim}\right\| = \sqrt{\tfrac{2}{3}}\left(a_4^{\mathrm{S}} + \bar{a}\right). \quad (6.46)$$

The specific form of $h_\alpha(c)$ is inspired by Fig. 6.16(b) and is equal to

$$h_\alpha = \left(\frac{0.5}{0.25 + (\mathbf{n}{:}\mathbf{n}_{\mathrm{z}} + 0.3)^2} + 0.209\mathbf{n}{:}\mathbf{n}_{\mathrm{z}} - 0.467\right)c + 1, \quad (6.47)$$

ROOSTAEI, 978-0-12-819293-1

LaTeX class: roostaei, 2021/05/25 10:02:47 roostaei driver • file: roostaei06.tex (Renata) • Prn: 2021/07/12;14:50:05 • p. 35
pro: ROOSTAEI • model: a03 • color: 1c • ref-style: Numbered (Style 1) • lang: en-US • docsubty: CHP •

B978-0-12-819293-1.00016-4, 00006

where $\mathbf{n}$ is the outer unit normal at the point of plastic straining, $\mathbf{n}_z$ is the unit director of distortion defined in Section 6.3.4, specifically in Algorithm 6.1. The term $\mathbf{n}:\mathbf{n}_z$ in Eq. (6.47) gives the directionality to the evolution of the backstress and thereby mimics the effect that yield surface distortion has on the strain without actually modeling yield surface distortion. Notice that $h_\alpha = 1$ when $c = 0$, so without the distortion, the nominal MAFTr KH rule is recovered. Moreover, $h_\alpha = 1$ is maintained during proportional loading when $\mathbf{n}:\mathbf{n}_z = \pm 1$ so as not to disturb the original calibration. The effect of the distortion modification is discussed in Section 6.4.3.

6.4 Numerical simulations and demonstrations

To study the role of yield surface distortion, the new model is used in three different settings:

1. **No distortion** ($c_0 = 0$, $h_\alpha = 1$). The model features nominal MAFTr KH rule by Dafalias and Feigenbaum [113]. With $c = 0$, the new yield function simply reduces to the von Mises.
2. **Directional distortion** ($c_0 > 0$, $h_\alpha = 1$). In this case the model keeps the original MAFTr KH rule. The new yield function manifests pronounced directional distortion.
3. **Distortion through kinematic hardening** that serves as a demonstration of the concept. With the evaluation of h_α the modified MAFTr KH rule from Section 6.3.6 imitates the presence of distortion despite maintaining von Mises sphere by holding $c_0 = 0$. With being only a demo concept, this setting is used in Fig. 6.20 only.

In this section, we briefly discuss how the model is implemented numerically, how it was calibrated, and then show simulations of cyclic loading with and without distortion.

6.4.1 Calibration from experimental data

A numerical calibration on a random uniaxial strain-controlled test in Fig. 6.18(a) was performed in order to identify the isotropic and kinematic hardening parameters related to a real material for use in further demonstrations. Elastic constants E, ν were chosen manually, using standard procedures in linear elasticity. The initial yield limit k_0 was chosen arbitrarily, as its influence is low due to isotropic softening driven by parameters κ_1 and κ_2. The hardening parameters were found using the Nelder–Mead method applied on the error function S defined by the least square method on the model stress response. As the MAFTr KH rule does not have the capability to demonstrate initial plateau, 48 initial data points have been removed from the minimizing function, leaving 301 active.

Severe deficiencies in stress response following short reverse loading cause poor concordance in further straining. Overall, models missing required features

ROOSTAEI, 978-0-12-819293-1

LaTeX class: roostaei, 2021/05/25 10:02:47 roostaei driver • file: roostaei06.tex (Renata) • Prn: 2021/07/12;14:50:05 • p. 36
pro: ROOSTAEI • model: a03 • color: 1c • ref-style: Numbered (Style 1) • lang: en-US • docsubty: CHP •

B978-0-12-819293-1.00016-4, 00006

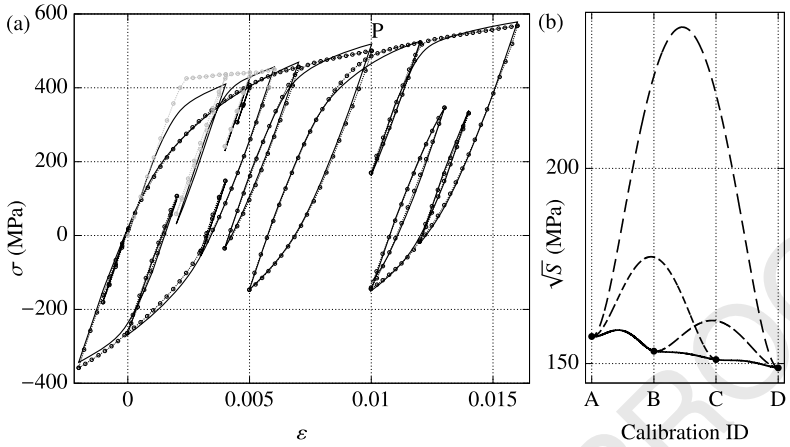

Figure 6.18 (a) Random uniaxial loading of C60R steel. (b) Inspection of the error function.

that are present in the experimental data require close monitoring of the calibration process, otherwise the solution will not represent a good approximation in any part of the calibrated trajectory. Four points A, B, C, and D with positions $\{X_A, X_B, X_C, X_D\}$ in the parameter space with values of the aggregate error $\sqrt{S_\alpha} = \{156.9, 153.2, 151.0, 148.9\}$ MPa were recorded during the final part of the calibration process. Several hundred successful iterations were reached between each of these points. Two of them are described in Table 6.2. Calibration marked D is used in further testing since it had the lowest error.

Calibration of parameters for the distortion is difficult without a sufficiently rich body of experimental data containing biaxial cyclic tests, as well as yield surface shape tracing. Therefore, the included distortion parameters are estimated. The possible inclusion of distortion parameters into a numerical calibration process can only be limited and will be the subject of future work.

To have some sense of the properties of the multidimensional error function S, linear probes into the parametric space were evaluated between points A, B, C, and D. The courses of the error function on lines connecting pairs of these points are shown in Fig. 6.18(b). This very limited insight shows the function is smooth within the region of acceptable parameters. No discontinuities were found. Still, numerical calculation for the gradient method may require further investigation into its feasibility due to potential impact of numerical tolerances. Concave regions of function S between points suggest the calibration proceeded down a thin, curved valley leading to the local minimum D. During calibration, periodic restarts were triggered with slowly decreasing size of the initial simplex to overcome slow convergence rate. The overall behavior implies the presence of thin steep valleys that can also be expected, as each of the parameters a_i^S representing the asymptotic limits of the backstress components acts with strong effect on the overall error and any change has to be carefully counterbalanced by the others. The error function is expected to have many local minima, since switching the order of backstress components produces the same result for $c_0 = 0$, while a

ROOSTAEI, 978-0-12-819293-1

LaTeX class: roostaei, 2021/05/25 10:02:47 roostaei driver • file: roostaei06.tex (Renata) • Prn: 2021/07/12;14:50:05 • p. 37
pro: ROOSTAEI • model: a03 • color: 1c • ref-style: Numbered (Style 1) • lang: en-US • docsubty: CHP •

B978-0-12-819293-1.00016-4, 00006

Table 6.2 Two calibrations A, D of MAFTr KH rule for the C60R steel.

	E [MPa]	ν	a_1^S [MPa]	a_2^S [MPa]	a_3^S [MPa]	a_4^S [MPa]	$\bar{a}$ [MPa]
A	195,000	0.3	127.169	134.452	437.245	80.2871	83.6503
D	195,000	0.3	127.249	135.184	655.890	35.6308	76.4801
	k_0 [MPa]	κ_1 [MPa]	κ_2^{-1} [MPa]	c_1^α[-]	c_2^α[-]	c_3^α[-]	c_4^α[-]
A	200	35,943.7	93.6811	5573.15	652.464	15.8642	251.807
D	200	38.775.9	94.8551	5461.59	641.735	15.4396	485.251
DDH	c_0[-]	c_1[-]	c_2[-]	c_3[-]	c_4[-]	c_5[-]	
	0.003	1.5	0.25	0.5	1.3	-0.5	

better fit can hardly be expected somewhere in-between due to the naturally appearing hierarchy of evolution rates of individual components.

6.4.2 Few remarks on numerical implementation

Satisfactory results were acquired using Euler forward scheme with stress correction. A modified midpoint rule was used, which is suitable for kinematic hardening rules with a high gradient of plastic modulus. As the numerical implementation is discussed elsewhere in this book, we can explore varying numerical accuracy related to distorted yield surface. Such phenomena are best observed on detailed high-resolution maps of numerical error and are relevant for any internal variable or their derivative.

The initial plastic state of the material, point P in Fig. 6.18(a) with calibration set D, is chosen and the field of normalized relative error is calculated according to the definition

$$\eta = \frac{\|\boldsymbol{\sigma} - \hat{\boldsymbol{\sigma}}\|}{k_0}, \tag{6.48}$$

where the examined stress response $\hat{\boldsymbol{\sigma}}$ is compared to the referential value $\boldsymbol{\sigma}$ obtained by a numerical calculation using the same scheme with $10\times$ lower tolerances and $10\times$ the number of strain increments with $10\times$ smaller integration steps within them. The size of strain increments for the examined response was 10^{-4} and the integration steps within were controlled so that backstress component increments norms did not exceed 7% of individual asymptotic norms.

Three initial points in the elastic region are chosen:

(a) Apex point on the main axis, see Fig. 6.19(a);
(b) Apex point on the main axis, see Fig. 6.19(b);
(c) A random point at the rear, see Fig. 6.19(c).

Fig. 6.19(a) shows the error field with loadings initiated directly from point P. A region of increased error is present in tangential direction to the yield surface. Because this region exhibits low plastic modulus, the error is incomparable with the situation in

ROOSTAEI, 978-0-12-819293-1

LaTeX class: roostaei, 2021/05/25 10:02:47 roostaei driver • file: roostaei06.tex (Renata) • Prn: 2021/07/12;14:50:05 • p. 38
pro: ROOSTAEI • model: a03 • color: 1c • ref-style: Numbered (Style 1) • lang: en-US • docsubty: CHP •

B978-0-12-819293-1.00016-4, 00006

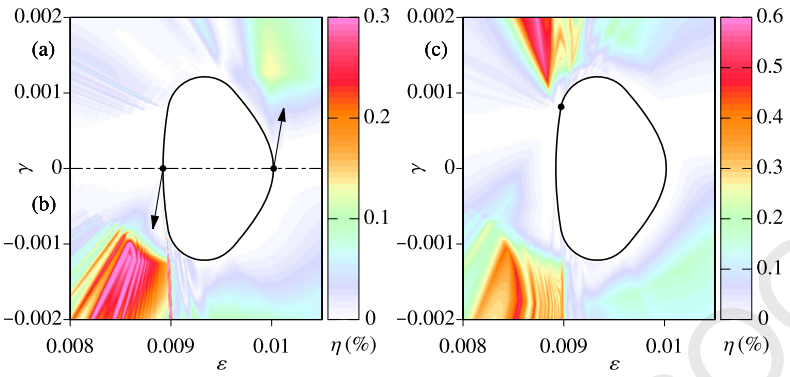

Figure 6.19 Numerical error in stress response with various initial point position: (a) symmetric field from the front apex, (b) symmetric field from the rear, and (c) general position.

Fig. 6.19(b), which initial point is at the rear of the yield surface. Very high value of plastic modulus increases numerical error considerably.

Even higher levels of numerical error were encountered in an asymmetric case in Fig. 6.19(c). Potential danger of straight regions of the yield surface profile lies in tangential trial strain increments. Small corrections of trial strain coming from an FE solver can induce large changes in the position of initial yield that can further induce large changes in the overall stress response, as the point of initial straining moves quickly along this straight region of YS. In this case, a custom KH rule employing the radial stress would be highly unstable.

Careful examination of these error maps brings new ideas considering optimizations of the integration step length. Problems uncovered this way may not be just of numerical nature, they may involve deficiencies of the fundamental theory of the model.

6.4.3 Preservation of the effect of distortion

In this subsection we evaluate how the kinematic distortion proposed in Section 6.3.6.1 can mimic the effect that DDH has on the plastic strain. From the experimental results in Fig. 6.4, a hypothetical yield surface with yield definition of 0.1% offset strain still demonstrates directional distortion. A simulation of such experiment, while keeping calibration D (Table 6.2), was performed with the new model in the initial point P (see Fig. 6.18) with the three different settings explained in Section 6.4.

The results in Fig. 6.20 provide us with several observations. With the nominal settings of **no distortion**, the equistrain map does not exhibit any form of distortion on either level of equivalent plastic strain. This may be expected, as the kinematic rule is quite simple, so there is no internal, implicit mechanism of the rule that would induce a more complex behavior.

With the model settings activating **directional distortion**, the isolines follow up the initial distortion of the yield surface. But the effect quickly diminishes, almost

ROOSTAEI, 978-0-12-819293-1

B978-0-12-819293-1.00016-4, 00006

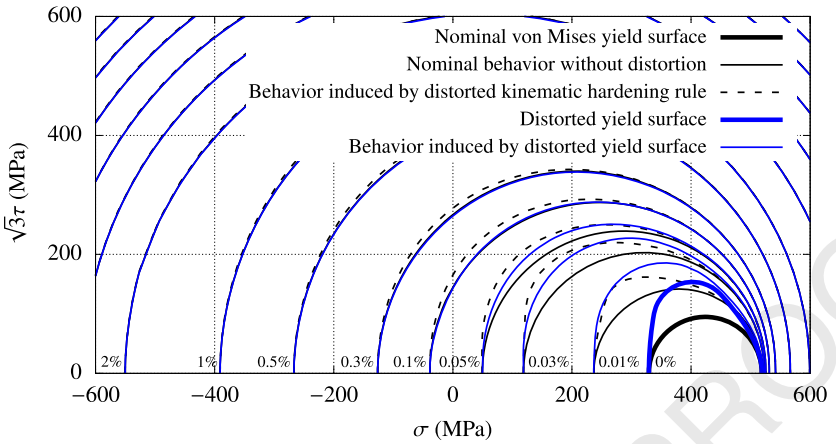

Figure 6.20 Isolines of equivalent cumulative plastic strain.

10× faster than the experimental results in Fig. 6.4. The two materials should be comparable to some degree and the deficiency of the distortional effect is strong. This suggests the suspected nature of distortion, proposed in Section 6.3.5, needs to be addressed in the kinematic rule as well.

The perceived distortion in the simulation with the level of cumulative plastic strain at 0.1% is all but nonexistent. The real effect in Fig. 6.4 is much more significant. It seems clear that for accurate prediction of the experiments the effect of yield surface distortion needs to be amplified by the kinematic hardening rules if, in fact, it is possible.

The proposed kinematic distortion applied on non distorted YS is depicted by dashed lines in Fig. 6.20. With higher intensity, the perceived distortion exhibits concavities. Perhaps with a more clever control the distorted kinematic hardening rule could show consistent distortion at even higher levels of equivalent strain. It definitely seems as a worthwhile addition to YS distortion and deserves additional investigation beyond the scope of this chapter.

6.4.4 Effect of distortion on biaxial ratcheting predictions

With the state-of-the-art kinematic hardening models, there are still some significant discrepancies between experiments and simulations of ratcheting. This is particularly true with biaxial ratcheting where the load is applied in two directions and at least one of the loads is cyclic. Unlike uniaxial ratcheting where the direction of plastic strain is the same as the direction of load, with biaxial ratcheting the direction of plastic strain must be predicted by a model.

Many believe the yield surface distortion may be the missing link to predicting ratcheting. Using the associative flow rule, as is usually the case with metals, the shape of the yield surface determines the direction of plastic strain increment, and thus the direction of the strains that accumulate during ratcheting. While yield surface

LaTeX class: roostaei, 2021/05/25 10:02:47 roostaei driver • file: roostaei06.tex (Renata) • Prn: 2021/07/12;14:50:05 • p. 40
pro: ROOSTAEI • model: a03 • color: 1c • ref-style: Numbered (Style 1) • lang: en-US • docsubty: CHP •

B978-0-12-819293-1.00016-4, 00006

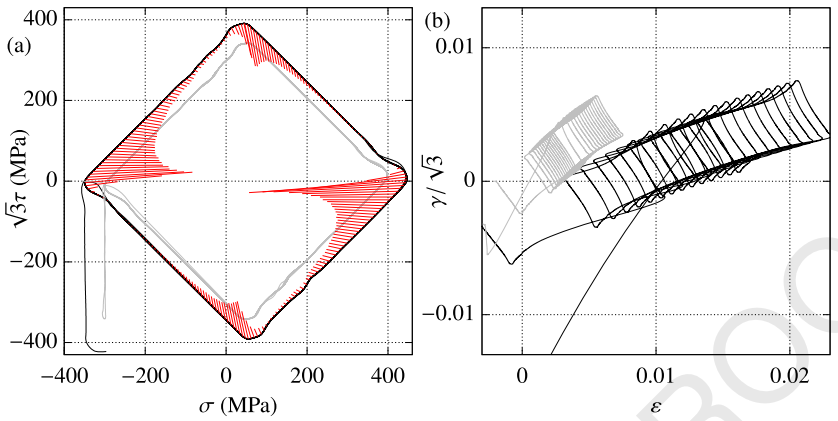

Figure 6.21 Biaxial ratcheting experiment after Halama et al. [115].

distortion is not the only way to affect the direction of the plastic strain increment, Bari and Hassan [4] suggest and Welling et al. [114] shows some evidence that yield surface distortion can improve ratcheting predictions. However, the results from [114] use a rather haphazard method of calibrating the plasticity model parameters and relatively little yield surface distortion so their evidence of that distortion improves predictions in ratcheting may just be coincidence.

Nonetheless, these results give some incentive for researchers to actively pursue yield surface distortion as a means to improve ratcheting predictions.

6.4.4.1 Tension–torsion biaxial ratcheting test

To better test how distortion affects ratcheting predictions, the newly derived model from Section 6.3.4 is used to predict a biaxial ratcheting experiment—a two-level rhombic stress path was chosen from Halama et al. [115].

In this experiment, a thin-walled tube of ST52 steel was cyclically loaded using stress control in both tension and torsion at two levels of amplitude. The load path for this experiment in stress and strain space is depicted in Fig. 6.21. Plastic flow rate direction and amplitude in the very last loop are depicted by red lines, mirrored inwards for convenience. For better concordance, only the second batch of loops depicted in black was evaluated by the calibration procedure.

Rather than calibrating the model on strain trajectory, the experiment was simulated with strain control. The overall ratcheting speed would otherwise dominate the evaluation of strain prediction error by the least square method and harm the evaluation of concordance of individual loops. Calibrating the model to fulfill known ratcheting speeds without sufficient concordance in stress space is very dangerous, as it could bring wildly different results in an actual real application where any form of validation is impossible.

As Fig. 6.22 shows, the distortional hardening had a negative effect in predicting the strain direction, when the limits in tension and compression were reached and the

LaTeX class: roostaei, 2021/05/25 10:02:47 roostaei driver • file: roostaei06.tex (Renata) • Prn: 2021/07/12;14:50:05 • p. 41
pro: ROOSTAEI • model: a03 • color: 1c • ref-style: Numbered (Style 1) • lang: en-US • docsubty: CHP •

B978-0-12-819293-1.00016-4, 00006

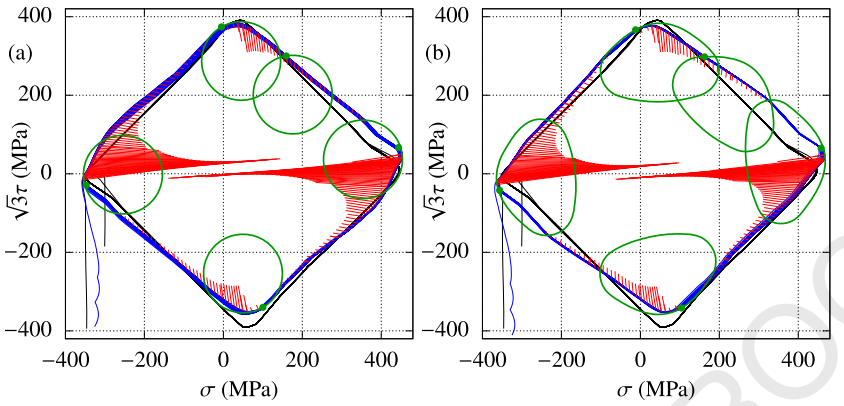

Figure 6.22 Two reverse simulations of a biaxial ratcheting experiment after Halama et al. [115].

slanted reversal was initially elastic. Upon leaving the elastic region, a kink in the stress response is visible, in the nondistorted and even more in the distorted model, greatly harming the stress concordance. The kink, behaving like a light beam leaving environment of higher refractive index, implies that the yield surface need to be even more distorted and therefore shorter, to reach almost orthogonal approach of the stress point to the yield surface.

6.4.4.2 Tension–hoop biaxial ratcheting test

A linear bow-tie loading trajectory from Corona et al. [116] is presented here. A tubular specimen of 1026 carbon steel is undergoing a cyclic strain-controlled tension of $\pm 0.5\%$ (x-axis) while with phase offset an internal pressure oscillates to induce between 50 and 85 MPa of hoop stress (θ). Fig. 6.23(b) shows the load path on a deviatoric stress plane. Note, that the tension dimension dominates the test in stress space. This test seems ideal for exploring multiaxial loading as it only subtly differs from a uniaxial experiment. The depicted evolution of the yield surface shows the return to von Mises sphere during reorientation of the distortion. A real material is not expected to have this induced unequal cross-effect. Simple modeling of such a behavior would require retaining some director of distortion during cyclic loading to orient this remaining distortion. A prolonged study into this encountered ideological problems that may only be solvable by advanced modeling methods.

To reproduce the butterfly experiment, the new model was calibrated according to stable hysteresis loop serving as material stabilization before the experiment. The calibration represented a perfect fit with parameters shown in Table 6.3. Reproduction of the biaxial experiment is shown in Fig. 6.23(a) with and without distortion. Rather than the uniform ratcheting speed shown by the experiment, the prediction exhibited slowdown from initially rapid plastic strain accumulation. Albeit with a different calibration, this behavior is consistent with predictions in Welling et al. [114]. Unfortunately, the activated distortion had only a negative effect in overestimating the

LaTeX class: roostaei, 2021/05/25 10:02:47 roostaei driver • file: roostaei06.tex (Renata) • Prn: 2021/07/12;14:50:05 • p. 42
pro: ROOSTAEI • model: a03 • color: 1c • ref-style: Numbered (Style 1) • lang: en-US • docsubty: CHP •

B978-0-12-819293-1.00016-4, 00006

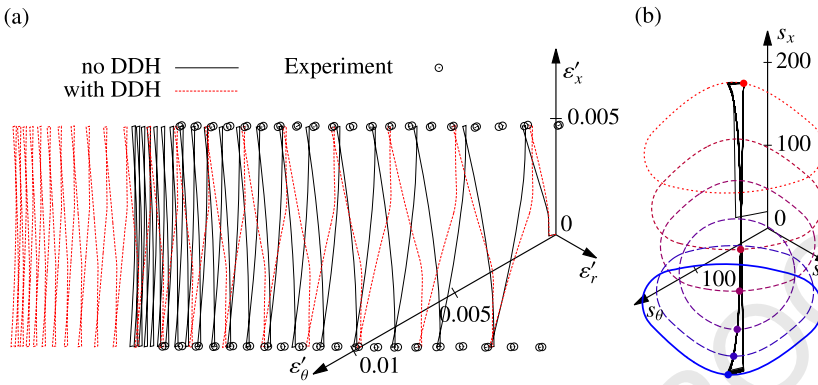

Figure 6.23 A simulation of the effect of distortion on bow-tie loading trajectory (20 loops) after Corona et al. [116]: (a) trajectory on the deviatoric plane in strain space, (b) trajectory on the deviatoric plane in stress space with yield surface evolution during a single loading segment.

Table 6.3 Three calibrations of MAFTr KH rule for biaxial ratcheting tests.

	E [MPa]	ν	a_1^S [MPa]	a_2^S [MPa]	a_3^S [MPa]	a_4^S [MPa]	$\bar{a}$ [MPa]
Rhombic noDDH	180,000	0.3	276.579	23.921	280.968	171.058	18.49
Rhombic DDH	180,000	0.3	53.0988	271.819	300.755	200.317	12.549
Tension–Hoop	170,000	0.3	84.1172	70.5965	7.87025	85.1375	352.968
	k_0 [MPa]	κ_1 [MPa]	κ_2^{-1} [MPa]	c_1^α[-]	c_2^α[-]	c_3^α[-]	c_4^α[-]
Rhombic noDDH	180	10,000	100.00	2785.18	205.616	22.682	8.201
Rhombic DDH	180	10,000	100.00	275.35	2662.68	16.32	9.5142
Tension–Hoop	100	-	k_0	5754.08	500.869	146.118	38.0204
DDH parameters	c_0[-]	c_1[-]	c_2[-]	c_3[-]	c_4[-]	c_5[-]	
Rhombic	3.836e–3	0.987	0.243	0.386	1.379	−0.347	
Tension–Hoop	0.018	1	0.25	0.4	1.3	−0.35	

ratcheting speed. A short inquiry of varying distortion parameters showed that the curvature of the front apex had only a limited effect on this behavior. This suggests that a major effect on the different prediction of ratcheting is the flat rear. Unlike a convex front, it is very sensitive on the orientation of the main axis of distortion. A correct simulation would therefore need a much deeper investigation. Further calibration of the model to the ratcheting speed did not bring satisfactory results.

6.5 Conclusions

Over the 20th century, experimental analysis of metal plasticity underwent rapid progress. Numerous methods and testing systems have been developed to examine plastic straining of metals under various conditions. Nowadays, distortion of yield surfaces is a recognized mechanism of strain hardening proved by many experimen-

LaTeX class: roostaei, 2021/05/25 10:02:47 roostaei driver • file: roostaei06.tex (Renata) • Prn: 2021/07/12;14:50:05 • p. 43
pro: ROOSTAEI • model: a03 • color: 1c • ref-style: Numbered (Style 1) • lang: en-US • docsubty: CHP •

B978-0-12-819293-1.00016-4, 00006

tal observations, independent of testing methodology and covering various metals and several other classes of materials. With additional experiments that use state-of-the-art testing systems with advanced computer control, it is possible that yield surface distortion and its evolution and its relation to plastic strain could be experimentally characterized with more accuracy and/or in more detail.

In this chapter, a new model was derived in order to test the effect that distortion of the yield surface has on ratcheting predictions. The new model proved itself capable of providing robust numerical predictions of yield surface distortion. However, initial evaluation suggests that this new model does not improve the ratcheting predictions in the cases studied in this chapter. That may be due to the calibration of the distortion, the kinematic rule used in conjunction with the distortion, the fact that only a single apex (a.k.a. uniaxial distortion) was considered, or several other factors. Detailed analysis of processes visible in the stress space, such as following the direction of plastic straining or even projecting an expected position of backstress on the basis of the associative rule, could help propose a dedicated kinematic hardening rule. There are many factors that impede such detailed approach, mainly the quality and smoothness of the experimental data, as well as the intensity of unwanted dynamic effects.

Despite all the experimental evidence of its presence, applying distortion to real life engineering simulations is still far in the future. The distortion should manifest in two ways: it should impact the direction of plastic flow, and it should limit the scope of elastic deformation within the expected elastic region. Both of these phenomena could be explicitly targeted in dedicated experiments. A flattened rear provides different directions of plastic flow in comparison to a von Mises sphere, and highly convex sides of the yield surface should induce a response highly sensitive on the exact direction of loading. Ratcheting speed of a well-defined experiment featuring amplitudes mildly exceeding the boundary of an expected elastic region should strongly indicate the presence of distortional hardening.

Pursuing the research into distortion by means of kinematic hardening or representative directions could be beneficial towards improving predictions, even if it means imitating presence of an actual distorted yield surface. Overall, while experiments show that yield surface distortion is clearly present, how this distortion effect predictions and plastic strain accumulation is still not well understood, and there is still much work to be done to bridge that gap.

Acknowledgments

This work was supported by the Czech Science Foundation (grant number GA19-03282S), by the Ministry of Education, Youth and Sports of the Czech Republic (Centre of Excellence for Nonlinear Dynamic Behaviour of Advanced Materials in Engineering—CeNDYNMAT, grant number CZ.-02.1.01/0.0/0.0/15_003/0000493; INTER-ACTION, LTA USA 18199), by the US Army Research Laboratory and the US Army Research Office under Grant No. W911NF-19-1-0040, and by the Institute of Thermomechanics of the Czech Academy of Sciences (grant number RVO:61388998).

LaTeX class: roostaei, 2021/05/25 10:02:47 roostaei driver • file: roostaei06.tex (Renata) • Prn: 2021/07/12;14:50:05 • p. 44
pro: ROOSTAEI • model: a03 • color: 1c • ref-style: Numbered (Style 1) • lang: en-US • docsubty: CHP •

B978-0-12-819293-1.00016-4, 00006

References

[1] H.P. Feigenbaum, Y.F. Dafalias, Directional distortional hardening in metal plasticity within thermodynamics, International Journal of Solids and Structures 44 (22) (2007) 7526–7542.
[2] Y.F. Dafalias, Planar double-slip micromechanical model for polycrystal plasticity, Journal of Engineering Mechanics 119 (6) (1993) 1260–1284.
[3] H.P. Feigenbaum, Y.F. Dafalias, Directional distortional hardening at large plastic deformations, International Journal of Solids and Structures 51 (23–24) (2014) 3904–3918.
[4] S. Bari, T. Hassan, Anatomy of coupled constitutive models for ratcheting simulation, International Journal of Plasticity 16 (3) (2000) 381–409.
[5] H. Ishikawa, Subsequent yield surface probed from its current center, International Journal of Plasticity 13 (6–7) (1997) 533–549.
[6] Y.F. Dafalias, D. Schick, C. Tsakmakis, A simple model for describing yield surface evolution during plastic flow, in: K. Hutter, H. Baaser (Eds.), Deformation and Failure in Metallic Materials, in: Lecture Notes in Applied and Computational Mechanics, Springer, Berlin Heidelberg, 2003, pp. 169–201.
[7] F. Körber, H. Hoff, Ueber die Festigkeitseigenschaften and den Reißwinkel kaltgewalzter Metalle, Mitteilungen aus dem Kaiser-Wilhelm-Institut fuer Eisenforschung zu Duesseldorf 10 (1928) 175–187.
[8] M. Cook, Directional properties in rolled brass strip, Journal of the Institute of Metals 60 (1937) 159–172.
[9] L.J. Klinglert, G. Sachs, Plastic flow characteristics of aluminum-alloy plate, Journal of the Aeronautical Sciences 15 (10) (1948) 599–604, https://doi.org/10.2514/8.11662.
[10] R. Hill, A theory of the yielding and plastic flow of anisotropic metals, Proceedings of the Royal Society of London A: Mathematical, Physical and Engineering Sciences 193 (1033) (1948) 281–297, http://rspa.royalsocietypublishing.org/content/193/1033/281.
[11] P.M. Naghdi, F. Essenburg, W. Koff, Experimental study of initial and subsequent yield surface in plasticity, Journal of Applied Mechanics 201 (25) (1958) 201.
[12] H.G. McComb, Some experiments concerning subsequent yield surfaces in plasticity, Tech. Rep. D-396, National Aeronautics and Space Administration, 1960.
[13] H.J. Ivey, Plastic stress–strain relations and yield surfaces for aluminum alloys, Journal of Mechanical Engineering and Sciences 3 (1) (1961) 15–31, https://doi.org/10.1243/JMES_JOUR_1961_003_005_02.
[14] W.A. Szczepiński, On the effect of plastic deformation on yield criterion, Archives of Mechanics 15 (2) (1963) 275–296.
[15] W.M. Mair, H.L.D. Pugh, Effect of pre-strain on yield surfaces in copper, Journal of Mechanical Engineering Science 6 (2) (1964) 150–163, http://jms.sagepub.com/content/6/2/150.full.pdf+html.
[16] S.B. Batdorf, B. Budiansky, A mathematical theory of plasticity based on the concept of slip, Tech. Rep. 1871, National Advisory Committee for Aeronautics, 1949.
[17] S. Hecker, Experimental investigation of corners in the yield surface, Acta Mechanica 13 (1–2) (1972) 69–86, https://doi.org/10.1007/BF01179659.
[18] M. Michno, W. Findley, An historical perspective of yield surface investigations for metals, International Journal of Non-Linear Mechanics 11 (1) (1976) 59–82.
[19] T. Kuwabara, Advances in experiments on metal sheets and tubes in support of constitutive modeling and forming simulations, International Journal of Plasticity 23 (3) (2007) 385–419.

ROOSTAEI, 978-0-12-819293-1

LaTeX class: roostaei, 2021/05/25 10:02:47 roostaei driver • file: roostaei06.tex (Renata) • Prn: 2021/07/12;14:50:05 • p. 45
pro: ROOSTAEI • model: a03 • color: 1c • ref-style: Numbered (Style 1) • lang: en-US • docsubty: CHP •

B978-0-12-819293-1.00016-4, 00006

[20] A. Phillips, C. Liu, J. Justusson, An experimental investigation of yield surfaces at elevated temperatures, Acta Mechanica 14 (2–3) (1972) 119–146, https://doi.org/10.1007/BF01184853.
[21] A. Phillips, J.-L. Tang, The effect of loading path on the yield surface at elevated temperatures, International Journal of Solids and Structures 8 (1972) 463–474.
[22] A. Phillips, W. Lu, An experimental investigation of yield surfaces and loading surfaces of pure aluminum with stress-controlled and strain-controlled paths of loading, Journal of Engineering Materials and Technology 106 (4) (1984) 349–354, https://doi.org/10.1115/1.3225729.
[23] H.C. Wu, W.C. Yeh, On the experimental determination of yield surfaces and some results on annealed 304 stainless steel, International Journal of Plasticity 7 (8) (1991) 803–826.
[24] H. Wu, J. Lu, W. Pan, Some observations on yield surfaces for 304 stainless steel at large prestrain, Journal of Applied Mechanics 62 (3) (1995) 626–632, https://doi.org/10.1115/1.2895992.
[25] S. Sung, L. Liu, H. Hong, H. Wu, Evolution of yield surface in the 2D and 3D stress spaces, International Journal of Solids and Structures 48 (6) (2011) 1054–1069.
[26] G.-L. Liu, S.-H. Huang, C.-S. Shi, B. Zeng, K.-S. Zhang, X.-C. Zhong, Experimental investigations on subsequent yield surface of pure copper by single-sample and multi-sample methods under various pre-deformation, Materials 11 (2) (2018), https://www.mdpi.com/1996-1944/11/2/277.
[27] Y. Ohashi, K. Kawashima, T. Yokochi, Anisotropy due to plastic deformation of initially isotropic mild steel and its analytical formulation, Journal of the Mechanics and Physics of Solids 23 (4) (1975) 277–294.
[28] A. Phillips, G.A. Gray, Experimental investigation of corners in the yield surface, Journal of Basic Engineering – Transactions of the ASME 83 (1961) 275–288.
[29] P. Theocaris, C. Hazell, Experimental investigation of subsequent yield surfaces using the moiré method, Journal of the Mechanics and Physics of Solids 13 (5) (1965) 281–294.
[30] W. Szczepiński, J. Miastkowski, An experimental study of the effect of the prestraining history on the yield surfaces of an aluminium alloy, Journal of the Mechanics and Physics of Solids 16 (3) (1968) 153–162, https://doi.org/10.1016/0022-5096(68)90024-0.
[31] J.F. Williams, N.L. Svensson, Effect of tensile prestrain on the yield locus of 1100-f alluminium, Journal of Strain Analysis 5 (2) (1970) 128–139.
[32] J.F. Williams, N.L. Svensson, A rationally based yield criterion for work hardening materials, Meccanica 6 (2) (1971) 104–114, https://doi.org/10.1007/BF02151650.
[33] E. Shiratori, K. Ikegami, K. Kaneko, The influence of the Bauschinger effect on the subsequent yield condition, Bulletin of JSME 16 (100) (1973) 1482–1493, http://ci.nii.ac.jp/naid/110002362076/en/.
[34] M. Michno, W. Findley, Subsequent yield surface for annealed mild steel under dead-weight loading – Aging, normality, convexity, corners, Bauschinger, and cross effect, Journal of Engineering Materials and Technology 96 (1) (1974) 56–64.
[35] E. Shiratori, K. Ikegami, F. Yoshida, K. Kaneko, S. Koike, The subsequent yield surfaces after preloading under combined axial load and torsion, Bulletin of the JSME 19 (134) (1976) 877–883.
[36] L. Ascione, R.S. Olivito, G. Spadea, An experimental study on subsequent yield surfaces for metals, Matériaux et Construction 15 (1) (1982) 21–26, https://doi.org/10.1007/BF02473555.
[37] J.R. Ellis, D.N. Robinson, C.E. Pugh, Time dependence in biaxial yield of type 316 stainless steel at room temperature, Journal of Engineering Materials and Technology 105 (4) (1983) 250–256, https://doi.org/10.1115/1.3225654.

LaTeX class: roostaei, 2021/05/25 10:02:47 roostaei driver • file: roostaei06.tex (Renata) • Prn: 2021/07/12;14:50:05 • p. 46
pro: ROOSTAEI • model: a03 • color: 1c • ref-style: Numbered (Style 1) • lang: en-US • docsubty: CHP •

B978-0-12-819293-1.00016-4, 00006

[38] A. Troshchenko, N. Kul'chitskii, An experimental investigation of the initial and subsequent yield surfaces of 40kh steel, Strength of Materials 15 (11) (1983) 1590–1595, https://doi.org/10.1007/BF01523566.
[39] A. Phillips, P.K. Das, Yield surfaces and loading surfaces of aluminum and brass: an experimental investigation at room and elevated temperatures, International Journal of Plasticity 1 (1) (1985) 89–109.
[40] M.G. Stout, P.L. Martin, D.E. Helling, G.R. Canova, Multiaxial yield behavior of 1100 aluminum following various magnitudes of prestrain, International Journal of Plasticity 1 (2) (1985) 163–174.
[41] D. Helling, A. Miller, M. Stout, An experimental investigation of the yield loci of 1100-0 aluminum, 70:30 brass, and an overaged 2024 aluminum alloy after various prestrains, Journal of Engineering Materials and Technology 108 (4) (1986) 313–320, https://doi.org/10.1115/1.3225888.
[42] H.C. Wu, J.C. Yao, S.C. Chu, Investigation of endochronic constitutive equation subject to plastic strain-controlled axial-torsional deformation, Journal of Engineering Materials and Technology 108 (3) (1986) 262–269.
[43] S. Cheng, E. Krempl, Experimental determination of strain-induced anisotropy during nonproportional straining of an Al/Mg alloy at room temperature, International Journal of Plasticity 7 (8) (1991) 827–846, https://doi.org/10.1016/0749-6419(91)90020-Y.
[44] A.S. Khan, X. Wang, An experimental study on subsequent yield surface after finite shear prestraining, International Journal of Plasticity 9 (8) (1993) 889–905.
[45] M. Boucher, P. Cayla, J.P. Cordebois, Experimental studies of yield surfaces of aluminium alloy and low carbon steel under complex biaxial loading, European Journal of Mechanics – A/Solids 14 (1) (1995) 1–17.
[46] L. Dietrich, Z.L. Kowalewski, Experimental investigation of an anisotropy in copper subjected to predeformation due to constant and monotonic loadings, International Journal of Plasticity 13 (1–2) (1997) 87–109.
[47] C. Lissenden, B. Lerch, J. Ellis, D. Robinson, Experimental determination of yield and flow surfaces under axial-torsional loading, in: S. Kalluri, P. Bonacuse (Eds.), Multiaxial Fatigue and Deformation Testing Techniques, in: American Society for Testing and Materials Special Technical Publication, vol. 1280, American Society for Testing and Materials, 1997, pp. 92–112, symposium on Multiaxial Fatigue and Deformation Testing Techniques, Denver, CO, May 15, 1995, http://www.refdoc.fr/Detailnotice?idarticle=15448531.
[48] C. Gil, C. Lissenden, B. Lerch, Determination of yield in Inconel axial-torsional loading at temperatures up to 649 °C, Tech. Rep. TM—1998-208658, NASA, 1998.
[49] S. Dannemeyer, Zur Veränderung der Fließfläche von Baustahl bei mehrachsiger plastischer Wechselbeanspruchung, PhD thesis, Carolo-Wilhelmina University, Braunschweig, 1999.
[50] A.A. Brown, J. Casey, D. Nikkel Jr., Experiments conducted in the context of the strain-space formulation of plasticity, International Journal of Plasticity 19 (11) (2003) 1965–2005, Finite Plasticity and Viscoplasticity – Theoretical, Experimental and Computational Aspects.
[51] A.S. Khan, R. Kazmi, A. Pandey, T. Stoughton, Evolution of subsequent yield surfaces and elastic constants with finite plastic deformation. Part – I: a very low work hardening aluminum alloy (Al6061-T6511), International Journal of Plasticity 25 (9) (2009) 1611–1625, Exploring New Horizons of Metal Forming Research.
[52] G. Hu, K. Zhang, S. Huang, J.-W.W. Ju, Yield surfaces and plastic flow of 45 steel under tension–torsion loading paths, Acta Mechanica Solida Sinica 25 (4) (2012) 348–360.

LaTeX class: roostaei, 2021/05/25 10:02:47 roostaei driver • file: roostaei06.tex (Renata) • Prn: 2021/07/12;14:50:05 • p. 47
pro: ROOSTAEI • model: a03 • color: 1c • ref-style: Numbered (Style 1) • lang: en-US • docsubty: CHP •

B978-0-12-819293-1.00016-4, 00006

[53] J.J. Guest, On the strength of ductile materials under combined stress, The London, Edinburgh, and Dublin Philosophical Magazine and Journal of Science 50 (302) (1900) 69–132, https://doi.org/10.1080/14786440009463892.
[54] R. Hill, The Mathematical Theory of Plasticity, Oxford University Press, 1950.
[55] K. Ikegami, An historical perspective of the experimental study of subsequent yield surfaces for metals. Part I, Japan Society of Materials Science 24 (261) (1975) 491–505; English translation BISI 14420, Sept. 1976.
[56] K. Ikegami, An historical perspective of the experimental study of subsequent yield surfaces for metals. Part II, Japan Society of Materials Science 24 (263) (1975) 709–719; English translation BISI 14420, Sept. 1976.
[57] S.S. Hecker, Experimental studies of yield phenomena in biaxially loaded metals, American Society of Mechanical Engineers (1976) 1–33, http://www.osti.gov/scitech/servlets/purl/7128705.
[58] K. Ikegami, Experimental plasticity on the anisotropy of metals, in: J.-P. Boehler (Ed.), Mechanical Behavior of Anisotropic Solids (Comportment Méchanique des Solides Anisotropes), Springer, Netherlands, Dordrecht, 1982, pp. 201–242, proceedings of the Euromech Colloquium 115 Villard-de-Lans, June 19–22, 1979.
[59] J.F. Bell, The experimental foundations of solid mechanics, in: C.A. Truesdell (Ed.), Mechanics of Solids, Springer-Verlag, Berlin, 1984, p. 813.
[60] A. Phillips, A review of quasistatic experimental plasticity and viscoplasticity, International Journal of Plasticity 2 (4) (1986) 315–328.
[61] W. Szczepiński, Experimental Methods in Mechanics of Solids, Elsevier, Amsterdam, 1990.
[62] M.G. Stout, U.F. Kocks, Effects of texture on plasticity, in: U.F. Kocks, C.N. Tome, H.-R. Wenk (Eds.), Texture and Anisotropy, Cambridge University Press, Cambridge, 1998, pp. 420–465.
[63] D.L. McDowell, Modeling and experiments in plasticity, International Journal of Solids and Structures 37 (1) (2000) 293–309.
[64] W. Lode, Versuche über den Einfluß der mittleren Hauptspannung auf das Fließen der Metalle Eisen, Kupfer und Nickel, Zeitschrift für Physik 36 (11) (1926) 913–939, https://doi.org/10.1007/BF01400222.
[65] L.W. Hu, J.F. Bratt, Effect of tensile plastic deformation on yield condition, Journal of Applied Mechanics 25 (1958) 411.
[66] A.S. Khan, A. Pandey, T. Stoughton, Evolution of subsequent yield surfaces and elastic constants with finite plastic deformation. Part III: yield surface in tension–tension stress space (Al 6061–T 6511 and annealed 1100 Al), International Journal of Plasticity 26 (10) (2010) 1432–1441.
[67] F. Rotvel, Biaxial fatigue tests with zero mean stresses using tubular specimens, International Journal of Mechanical Sciences 12 (7) (1970) 597–613.
[68] G.I. Taylor, H. Quinney, The plastic distortion of metals, Philosophical Transactions of the Royal Society of London A: Mathematical, Physical and Engineering Sciences 230 (681–693) (1931) 323–362, http://rsta.royalsocietypublishing.org/content/230/681-693/323.
[69] R. Schmidt, Über den Zusammenhang von Spannungen und Formänderungen im Verfestigungsgebiet, Ingenieur-Archiv 3 (3) (1932) 215–235, https://doi.org/10.1007/BF02079970.
[70] J.L.M. Morrison, The criterion of 'yield' of gun steels, Proceedings of the Institution of Mechanical Engineers 159 (1) (1948) 81–94, https://doi.org/10.1243/PIME_PROC_1948_159_012_02.

ROOSTAEI, 978-0-12-819293-1

LaTeX class: roostaei, 2021/05/25 10:02:47 roostaei driver • file: roostaei06.tex (Renata) • Prn: 2021/07/12;14:50:05 • p. 48
pro: ROOSTAEI • model: a03 • color: 1c • ref-style: Numbered (Style 1) • lang: en-US • docsubty: CHP •

B978-0-12-819293-1.00016-4, 00006

[71] P.M. Naghdi, J.C. Rowley, C.W. Beadle, Experiments concerning the yield surface and the assumption of linearity in the plastic stress–strain relations, Journal of Applied Mechanics 22 (1955) 416–420.

[72] P.K. Bertsch, W.N. Findley, An experimental study of subsequent yield surfaces – corners, normality, Bauschinger effect and allied effect, in: Proceedings of 4th U.S. National Congress of Applied Mechanics, 1962, pp. 893–907.

[73] B. Paul, W. Chen, L. Lee, An experimental study of plastic flow under stepwise increments of tension and torsion, in: Proceedings of 4th U.S. National Congress of Applied Mechanics 2, 1962, pp. 1031–1038.

[74] E. Shiratori, K. Ikegami, Experimental study of the subsequent yield surface by using cross-shaped specimens, Journal of the Mechanics and Physics of Solids 16 (6) (1968) 373–394.

[75] J. Parker, M.B. Bassett, Plastic stress–strain relationships – some experiments to derive a subsequent yield surface, Journal of Applied Mechanics 31 (4) (1964) 676–682, https://doi.org/10.1115/1.3629730.

[76] ASTM E111-97, Standard Test Method for Young's Modulus, Tangent Modulus, and Chord Modulus, ASTM International, West Conshohocken, PA, 1997, www.astm.org, http://www.astm.org/cgi-bin/resolver.cgi?E111-97.

[77] N. Gupta, H. Lauert, A study of yield surface upon reversal of loading under biaxial stress, ZAMM – Journal of Applied Mathematics and Mechanics (Zeitschrift für Angewandte Mathematik und Mechanik) 63 (10) (1983) 497–504, https://doi.org/10.1002/zamm.19830631005.

[78] H.-C. Wu, Effect of loading-path on the evolution of yield surface for anisotropic metals subjected to large pre-strain, International Journal of Plasticity 19 (10) (2003) 1773–1800.

[79] A.S. Khan, R. Kazmi, B. Farrokh, Multiaxial and non-proportional loading responses, anisotropy and modeling of Ti–6Al–4V titanium alloy over wide ranges of strain rates and temperatures, International Journal of Plasticity 23 (6) (2007) 931–950.

[80] A.S. Khan, S. Yu, Deformation induced anisotropic responses of Ti–6Al–4V alloy. Part I: experiments, International Journal of Plasticity 38 (2012) 1–13.

[81] A.S. Khan, S. Yu, H. Liu, Deformation induced anisotropic responses of Ti–6Al–4V alloy. Part II: a strain rate and temperature dependent anisotropic yield criterion, International Journal of Plasticity 38 (2012) 14–26.

[82] S. Kolling, A. Haufe, M. Feucht, P.A. Du Bois, SAMP-1: a semi-analytical model for the simulation of polymers, in: 4. LS-DYNA Anwenderforum, Bamberg, 2005, p. 26.

[83] J.M. Pestana, A.J. Whittle, Formulation of a unified constitutive model for clays and sands, International Journal for Numerical and Analytical Methods in Geomechanics 23 (12) (1999) 1215–1243.

[84] M. Taiebat, Y.F. Dafalias, SANISAND: simple anisotropic sand plasticity model, International Journal for Numerical and Analytical Methods in Geomechanics 32 (8) (2008) 915–948, https://onlinelibrary.wiley.com/doi/abs/10.1002/nag.651.

[85] Y.-P. Yao, Y.-X. Kong, Extended UH model: three-dimensional unified hardening model for anisotropic clays, Journal of Engineering Mechanics 138 (7) (2012) 853–866, https://ascelibrary.org/doi/abs/10.1061/%28ASCE%29EM.1943-7889.0000397.

[86] F. Edelman, D.C. Drucker, Some extensions of elementary plasticity theory, Journal of the Franklin Institute 251 (6) (1951) 581–605.

[87] A. Baltov, A. Sawczuk, A rule of anisotropic hardening, Acta Mechanica 1 (2) (1965) 81–92, https://doi.org/10.1007/BF01174305.

LaTeX class: roostaei, 2021/05/25 10:02:47 roostaei driver • file: roostaei06.tex (Renata) • Prn: 2021/07/12;14:50:05 • p. 49
pro: ROOSTAEI • model: a03 • color: 1c • ref-style: Numbered (Style 1) • lang: en-US • docsubty: CHP •

B978-0-12-819293-1.00016-4, 00006

[88] D.E. Helling, A.K. Miller, The incorporation of yield surface distortion into a unified constitutive model, Part I: equation development, Acta Mechanica 69 (1–4) (1987) 9–23, https://doi.org/10.1007/BF01175711.
[89] H.-C. Wu, H.-K. Hong, J.-K. Lu, An endochronic theory accounted for deformation induced anisotropy, International Journal of Plasticity 11 (2) (1995) 145–162.
[90] A.K. Mālmeisters, Geometry of theories of strength, Mechanics of Polymers 4 (1966) 519–526 (in Russian).
[91] I.I. Gol'denblat, V.A. Kopnov, Criteria of Strength and Plasticity in Construction Materials, Mashinostroenie, Moscow, 1968 (in Russian).
[92] D.W.A. Rees, An examination of yield surface distortion and translation, Acta Mechanica 52 (1) (1984) 15–40, https://doi.org/10.1007/BF01175962.
[93] G. Grewolls, R. Kreißig, Anisotropic hardening – numerical application of a cubic yield theory and consideration of variable r-values for sheet metal, European Journal of Mechanics – A/Solids 20 (4) (2001) 585–599.
[94] A.V. Shutov, S. Panhans, R. Kreissig, A phenomenological model of finite strain viscoplasticity with distortional hardening, ZAMM – Zeitschrift für angewandte Mathematik und Mechanik 91 (8) (2011) 653–680.
[95] V.I. Danilov, On the formulation of the law of distortional hardening, Mechanics of Solids 6 (1971) 146–150, in Russian.
[96] B.T. Lester, W.M. Scherzinger, An evolving effective stress approach to anisotropic distortional hardening, International Journal of Solids and Structures 143 (2018) 194–208, https://doi.org/10.1016/j.ijsolstr.2018.03.007.
[97] H.P. Feigenbaum, Y.F. Dafalias, Simple model for directional distortional hardening in metal plasticity within thermodynamics, Journal of Engineering Mechanics 134 (9) (2008) 730–738.
[98] S. Parma, J. Plešek, R. Marek, Z. Hrubý, H.P. Feigenbaum, Y.F. Dafalias, Calibration of a simple directional distortional hardening model for metal plasticity, International Journal of Solids and Structures 143 (2018) 113–124.
[99] M. Ortiz, E.P. Popov, Distortional hardening rules for metal plasticity, Journal of Engineering Mechanics 109 (4) (1983) 1042–1057.
[100] M. François, A plasticity model with yield surface distortion for non proportional loading, International Journal of Plasticity 17 (5) (2001) 703–717.
[101] A.V. Shutov, J. Ihlemann, A viscoplasticity model with an enhanced control of the yield surface distortion, International Journal of Plasticity 39 (2012) 152–167.
[102] W.-C. Yeh, C.-D. Ho, W.-F. Pan, An endochronic theory accounting for deformation induced anisotropy of metals under biaxial load, International Journal of Plasticity 12 (8) (1996) 987–1004.
[103] T. Kurtyka, M. Życzkowski, Evolution equations for distortional plastic hardening, International Journal of Plasticity 12 (2) (1996) 191–213.
[104] W. Prager, Recent developments in the mathematical theory of plasticity, Journal of Applied Physics 20 (3) (1949) 235–241, https://doi.org/10.1063/1.1698348.
[105] D.C. Drucker, R.E. Gibson, D. Henkel, Soil mechanics and work-hardening theories of plasticity, Transactions American Society of Civil Engineers 122 (1957) 338–346.
[106] J. Plešek, A. Křístek, Assessments of methods for locating the point of initial yield, Computer Methods in Applied Mechanics and Engineering 141 (3) (1997) 389–397.
[107] J. Plešek, H.P. Feigenbaum, Y.F. Dafalias, Convexity of yield surface with directional distortional hardening rules, Journal of Engineering Mechanics 136 (4) (2010) 477–484.
[108] R. Marek, J. Plešek, Z. Hrubý, S. Parma, H.P. Feigenbaum, Y.F. Dafalias, Numerical implementation of a model with directional distortional hardening, Journal of Engineering

ROOSTAEI, 978-0-12-819293-1

LaTeX class: roostaei, 2021/05/25 10:02:47 roostaei driver • file: roostaei06.tex (Renata) • Prn: 2021/07/12;14:50:05 • p. 50
pro: ROOSTAEI • model: a03 • color: 1c • ref-style: Numbered (Style 1) • lang: en-US • docsubty: CHP •

B978-0-12-819293-1.00016-4, 00006

Mechanics (ASCE) 141 (12) (2015) 04015048, https://ascelibrary.org/doi/abs/10.1061/(ASCE)EM.1943-7889.0000954.

[109] M. Zhang, J.M. Benítez, F.J. Montáns, Capturing yield surface evolution with a multilinear anisotropic kinematic hardening model, International Journal of Solids and Structures 81 (2016) 329–336.

[110] M. Freund, A.V. Shutov, J. Ihlemann, Simulation of distortional hardening by generalizing a uniaxial model of finite strain viscoplasticity, International Journal of Plasticity 36 (2012) 113–129.

[111] P.H. Dluzewski, The effect of slips on the anisotropic behaviour of polycrystalline aluminium at elevated temperature, Textures and Microstructures 19 (1–2) (1992) 81–99.

[112] F. Liu, Q. Fu, C. Chen, N. Liang, An elasto-plastic damage constitutive theory and its prediction of evolution of subsequent yield surfaces and elastic constants, International Journal of Plasticity 27 (9) (2011) 1355–1383.

[113] Y.F. Dafalias, H.P. Feigenbaum, Biaxial ratchetting with novel variations of kinematic hardening, International Journal of Plasticity 27 (4) (apr 2011) 479–491.

[114] C. Welling, R. Marek, H. Feigenbaum, Y. Dafalias, J. Plešek, Z. Hrubý, S. Parma, Numerical convergence in simulations of multiaxial ratcheting with directional distortional hardening, International Journal of Solids and Structures (2017) 105–121.

[115] R. Halama, M. Fusek, Z. Poruba, Influence of mean stress and stress amplitude on uniaxial and biaxial ratcheting of ST52 steel and its prediction by the Abdelkarim–Ohno model, International Journal of Fatigue 91 (2016) 313–321, Variable Amplitude Loading.

[116] E. Corona, T. Hassan, S. Kyriakides, On the performance of kinematic hardening rules in predicting a class of biaxial ratcheting histories, International Journal of Plasticity 12 (1) (1996) 117–145.

ROOSTAEI, 978-0-12-819293-1

LaTeX class: roostaei, 2021/05/25 10:02:47 roostaei driver • file: roostaei06.tex (Renata) • Prn: 2021/07/12;14:50:05 • p. 51
pro: ROOSTAEI • model: a03 • color: 1c • ref-style: Numbered (Style 1) • lang: en-US • docsubty: CHP •

B978-0-12-819293-1.00016-4, 00006

Non-Print Items

Abstract

When the associative flow rule is used, the yield surface (YS) shape is related to the direction of plastic strain accumulation. In this case, accurate modeling of the YS shape and its changes is critical to predicting the strains seen during cyclic plastic loading. There are numerous experimental examples of the shape of the YS changing such that a sharp apex develops roughly in the direction of loading and flattening develops in the opposite direction as anisotropy develops in the material. The growth of this type of uneven distortion of the YS has been seen in a wide variety of metals under various load conditions and is often called directional distortional hardening (DDH). In this chapter, we review the literature on DDH and YS shape change and present a new segmented model for DDH. We calibrated this model and used it to simulate a directionally distorted yield surface and cyclic plastic loading. By directly comparing results with and without YS distortion, we are able to infer the role that DDH has in predicting the behavior of metals in cyclic plastic loading.

Keywords

Yield surface shape, Distortion, Directional distortion, Directional distortional hardening, Anisotropy, Segmented yield function

LaTeX class: roostaei, 2021/05/25 10:02:47 roostaei driver • file: roostaei06.tex (Renata) • Prn: 2021/07/12;14:50:06 • p. 52
pro: ROOSTAEI • model: a03 • color: 1c • ref-style: Numbered (Style 1) • lang: en-US • docsubty: CHP •